Microbial iron(III) reduction during palsa collapse promotes greenhouse gas emissions before complete permafrost thaw

Monique S. Patzner[1], Merritt Logan[2], Amy M. McKenna[3], Robert B. Young[2,4], Zhe Zhou[1,5], Hanna Joss[1], Carsten W. Mueller[6,7], Carmen Hoeschen[6], Thomas Scholten[8], Daniel Straub[9,10], Sara Kleindienst[9], Thomas Borch[2], Andreas Kappler[1,11] & Casey Bryce[1,12]*

[1]Geomicrobiology, Center for Applied Geosciences, University of Tuebingen, Schnarrenbergstrasse 94-96, 72076 Tuebingen, Germany.

[2]Department of Soil & Crop Sciences and Department of Chemistry, Colorado State University, 307 University Ave, Fort Collins, CO, 80523-1170 US.

[3] National High Magnetic Field Laboratory, Florida State University, Tallahassee, FL 32310-4005, US.

[4]Chemical Analysis and Instrumentation Laboratory, New Mexico State University, P.O. Box 30001, MSC 3RES, Las Cruces, NM, 88003, US.

[5]Alfred-Wegener-Institute, Helmholtz Centre for Polar and Marine Research, Am Handelshafen 12, 27570 Bremerhaven, Germany

[6]Chair of Soil Science, TUM School of Life Sciences, Technical University of Munich, Emil-Ramann Strasse 2, 85354 Freising, Germany.

[7]Department of Geosciences and Natural Resource Management, University of Copenhagen, Øster Voldgade 10, 1350 Copenhagen, Denmark.

[8]Chair of Soil Science and Geomorphology, Rümelinstraße 19-23, 72070 Tübingen, University of Tuebingen, Germany.

[9]Microbial Ecology, Center for Applied Geosciences, University Tuebingen, Schnarrenbergstrasse 94-96, 72076 Tuebingen, Germany.

[10]Quantitative Biology Center (QBiC), University Tuebingen, Auf der Morgenstelle 10, 72076 Tuebingen, Germany.

[11] Cluster of Excellence: EXC 2124: Controlling Microbes to Fight Infection, Tübingen, Germany.

[12]School of Earth Sciences, University of Bristol, Wills Memorial Building, Queens Road Bristol BS8 1RJ, UK.

*Corresponding Author: Casey Bryce

Email: casey.bryce@bristol.ac.uk

This is a preprint submitted to Earth ArXiv and has not been peer reviewed

KEYWORDS: Soil organic carbon, iron, bioavailability, permafrost collapse, FT-ICR-MS, microbial Fe(III) reduction and Fe(II) oxidation, methane and carbon dioxide emissions, Abisko, Arctic, peatland

ABSTRACT:

Reactive iron (Fe) minerals can preserve organic carbon (OC) in soils overlying intact permafrost. With permafrost thaw, reductive dissolution of iron minerals releases Fe and OC into the porewater, potentially increasing the bioavailability of OC for microbial decomposition. However, the stability of this so-called rusty carbon sink, the microbial community driving mineral dissolution, the identity of the iron-associated carbon and the resulting impact on greenhouse gas emissions are unknown. We examined palsa hillslopes, gradients from intact permafrost-supported palsa to semi-wet partially-thawed bog in a permafrost peatland in Abisko (Sweden). Using high-resolution mass spectrometry, we found that Fe-bound OC in intact palsa is comprised of loosely bound more aliphatic and strongly-bound more aromatic species. Iron mineral dissolution by both fermentative and dissimilatory Fe(III) reduction releases Fe-bound OC along the palsa hillslopes, before complete permafrost thaw. The increasing bioavailability of dissolved OC (DOC) leads to its further decomposition, demonstrated by an increasing nominal oxidation state of carbon (NOSC) and a peak in bioavailable acetate (61.7±42.6 mg C/L) at the collapsing palsa front. The aqueous Fe^{2+} released is partially re-oxidized by Fe(II)-oxidizing bacteria but cannot prevent the overall loss of the rusty carbon sink with palsa collapse. The increasing relative abundance and activity of Fe(III)-reducers is accompanied by an increasing abundance of methanogens and a peak in methane (CH_4) emissions at the collapsing front. Our data suggest that the loss of the rusty carbon sink directly contributes to carbon dioxide (CO_2) production by Fe(III) reduction coupled to OC oxidation and indirectly to CH_4 emission by promoting methanogenesis even before complete permafrost thaw.

INTRODUCTION:

Climate change has enormous consequences for permafrost environments, causing rapid changes in soil conditions (such as thermal and moisture regime, and aeration) with direct consequences for organic (OC) destabilization[1]. Permafrost soils store ~60% of the world's soil OC in 15% of the global soil area[2,3]. This preserved OC will become increasingly exposed to microbial decomposition and thus can be released from the active layer to the atmosphere as greenhouse gases (GHGs) such as carbon dioxide (CO_2) and methane (CH_4)[4] or discharged by drainage[5]. However, the magnitude of the release of this OC depends strongly on a large variety of factors[6], including the hydrology, soil parent material, organic matter content and the ability of soil minerals to protect OC from degradation, which can regulate long-term preservation of OC[7].

Iron (Fe) minerals are known to stabilize organic carbon by sorption/co-precipitation and protect it from degradation by generating OC-Fe associations that are more persistent in soils[8,9, 10-13]. However, by providing a terminal electron acceptor for anaerobic respiration[14,15], Fe can also enhance decomposition. The fate of Fe and associated OC determines Fe-OC aggregate formation and ultimately accessibility for microbial decomposition[15, 16,17]. Reactive Fe-OC associations (defined as the solid Fe phases that are reductively dissolved by sodium dithionite[11,18,19]) have been shown to serve as an effective rusty carbon sink and to preserve OC over geological timescales[11]. Previously, it has been shown that reactive Fe-OC associations can mainly be found in intact permafrost soils[20], but cannot preserve OC along a permafrost thaw gradient, following complete permafrost thaw from palsa to bog to fen type wetlands[19]. However, the stability of Fe-OC associations during transitional processes along permafrost thaw gradients remain unstudied. The need to better understand the climate impact of transitional processes in thawing permafrost was stated previously by Shelef *et al.*[21] who

emphasize large uncertainty in permafrost carbon stocks (>200%) due to processes at collapsing fronts. Indeed, methane dynamics can also strongly differ between end-members and transitional thaw stages[22].

With permafrost thaw, soils become water-logged and oxygen (O_2) limited, favoring reductive dissolution of reactive Fe(III)[19]. Fe(III)-reducing microorganisms are able to use the reactive Fe(III) as an electron acceptor for anaerobic respiration and, depending on its composition, the associated OC as electron source, resulting in CO_2 and Fe(II) formation[22]. Thus, Fe(III) reduction directly contributes to CO_2 emissions[23]. Fe(III) reduction may also influence CH_4 emissions in thawing permafrost peatlands. On the one hand, Fe(III) reduction is thermodynamically more favorable and thus could outcompete methanogenesis[24]. On the other hand, Fe(III) reduction leads to proton consumption which results in an increasing pH that could favor methanogenesis[25]. The complex balance of these processes that either suppress or promote GHG emissions such as CO_2 and CH_4 highlights the need for a fundamental understanding of microbial Fe metabolisms and their interactions with methanotrophs and methanogens, which is currently lacking.

The release of previously Fe-associated OC into surrounding porewater following reductive dissolution could lead to further microbial decomposition of OC and emission of GHGs such as CO_2 and CH_4. Mineral-associated OC (MAOC) has been proposed to be comprised of low molecular weight compounds of microbial (e.g. microbial polysaccharides, amino sugars, muramic acid) and plant origin[13,26-30] with low activation energies of MAOC for degradation by microbes. Therefore, the release of MAOC with permafrost thaw is considered an important driver of the composition of arctic surface waters and microbial respiration[31,32]. Recent studies described carboxylic-rich[33] and aliphatic Fe-bound OC in forest soils as more resistant during reductive dissolution[34]. In Siberian permafrost soils, hydrophobic, aromatic DOC was preferentially sorbed by shallower, acidic soil horizons and correlated with an increasing

abundance of Fe oxides[35]. The identity of Fe-bound OC in permafrost environments, however, still remains unknown.

To understand the direct impact of the loss of this so called rusty carbon sink[36] on net GHG emissions in thawing permafrost peatlands, it is essential to further determine (1) the bioavailability of Fe-bound OC and released OC during permafrost thaw and (2) changes in the present and active microbial community, particularly the Fe(III)-reducing bacteria which are key players in reactive Fe mineral dissolution and their interplay with methanotrophs and methanogens.

We followed the dynamic biogeochemical interactions of Fe-OC associations in the active layer along collapsing palsa hillslopes, where palsas underlain by intact permafrost are collapsing into partially-thawed, semi-wet bogs. Fe-OC associations were characterized in the solid phase using selective extractions, scanning electron microscopy (SEM), nanoscale secondary ion mass spectrometry (nanoSIMS), and Mössbauer spectroscopy, and the effect of palsa collapse on porewater geochemistry and CO_2 and CH_4 fluxes was quantified. Reactive Fe-associated OC and DOC in the porewater along the palsa hillslope were investigated at the molecular-level with Fourier transform ion cyclotron resonance mass spectrometry (FT-ICR-MS), and the present and active microbial community was characterized using DNA- and RNA-based 16S rRNA amplicon (gene) sequencing.

RESULTS & DISCUSSION:

Greenhouse gas emissions promoted by microbial iron cycling in thawing permafrost peatlands. In the palsa and at the collapsing front (Figures S1 and S2), net CO_2 emissions measured from static flux chambers were similar on average (1.57±0.27 μmol/m^2/s) and slightly decreased in the bog to 1.12±0.51 μmol/m^2/s (Figure 1). Replicate analysis of CO_2 concentrations in automatic Eosense eosFD gas flux chambers showed similar CO_2 emissions along the palsa hillslope (Figure S3). Net CH_4 emissions were very low in the palsa (0.003±0.001 μmol/m^2/sec), significantly increased at the collapsing front to 0.025±0.001 μmol/m^2/s and then slightly decreased in the bog (0.013±0.001 μmol/m^2/s; Figure 1). Emission rates of CO_2 and CH_4 in the palsa and the bog are in line with previous studies at Stordalen mire [37-39], however, this is the first report of emissions at the collapsing front, where palsa is collapsing into the bog.

Previous work demonstrated that highest reactive Fe and associated OC contents can be found where the organic and mineral horizons meet, which we have termed the "transition zone"[19]. DOC concentrations in the porewater of the transition zone were low in the intact palsa (Palsa A, 57.97±16.49 mg/L). Porewater DOC significantly increased towards the collapsing front to 207.65±168.16 mg/L in the more collapsed palsa (Palsa B). Highest DOC concentrations were found directly at the collapsing front (535.75±131.45 mg/L) and then significantly decreased in the bog (279.62±113.14 to 206±80.28 mg/L) (Figure 1, Figure S1, Figure S4).

The aqueous Fe^{2+} concentrations show the same trend as the DOC (Figure 1). Aqueous Fe^{2+} concentrations in the palsa were lowest along the palsa hillslope (4.47±3.16 to 22.62±30.14 mg/L; Figure 1) and significantly increased at the collapsing front. Highest aqueous Fe^{2+} concentrations were measured at the collapsing front (153.24±40.14 mg/L) and significantly decreased again at the two measured locations in the bog to 48.86±11.43 and 82.43±47.93 mg/L

(Figure 1). Other elements such as dissolved phosphorous (P) also strongly correlated with the aqueous Fe^{2+} pulse at the collapsing front, suggestive of mineral dissolution and release of mineral-associated P (Figures S5- S6).

The release of OC and aqueous Fe^{2+} along the palsa hillslope was accompanied by an increase in the relative 16S rRNA gene sequence abundance (DNA-based) of iron- and methane-cycling microorganisms in the transition zone and mineral horizon from the palsa to the collapsing front (Figure 1; Figure S7). Towards the collapsing front, Fe(III)-reducing bacteria increased from 0.41±0.07 to 2.46±0.34% in the transition zone and from 0.21±0.05 to 2.42±0.27% in the mineral horizon (Figure 1). Fe(II)-oxidizing bacteria also increased from the palsa to the collapsing front from 0.54±0.26 to 2.33±0.33% in the transition zone and from 0.92±0.58 to 1.66±0.44% in the mineral horizon. Methanogens increased along the palsa hillslope from 0.42±0.37 to 2.83±0.26% in the transition zone and from 1.40±1.40 to 11.68±3.12% in the mineral horizon. Methanotrophs increased from the palsa to the collapsing front from 0.90±0.30 to 1.93±0.09% in the transition zone and from 0.58±0.08 to 1.26±0.29% in the mineral horizon (Figure 1). Along the palsa hillslope, the relative 16S rRNA gene sequence abundances of iron- and methane-cycling microorganisms were stable in the organic horizon (Figure 1). The iron- and methane-cycling microorganisms are described in detail in Figure 2. For estimated absolute abundances of bacteria and archaea as well as the manually-compiled database used to identify iron- and methane-cycling microorganisms and the whole microbial community see Figure 2 and SI (Figures S8 and S9 and Tables S1-S4).

This data reveals that the so-called rusty carbon sink is already destabilized during palsa collapse, even before complete permafrost thaw. Lateral flow by runoff of rain and/or melt water[40,41] in the transition zone between organic and mineral horizon, caused by bulk density shifts (organic horizon: 0.03±0.01 g/cm^3 and mineral horizon: 0.84±0.26 g/cm^3)[19], favors micro-oxic conditions, as also described for other permafrost hillslopes[42]. These redox conditions

promote microbial reduction of reactive Fe(III) minerals coupled to carbon oxidation [14,43]. This results in a release of Fe and Fe-associated OC into the surrounding porewater and ultimately contributes to a pulse of aqueous Fe^{2+} and DOC at the collapsing front – where we observed the highest aqueous Fe^{2+} and DOC concentrations ever measured along the whole thaw gradient[19]. The release of OC along the palsa hillslope results from multiple co-occurring processes. These include the release of Fe-associated OC, changes in pH[44], plant community[45] (Figure S10), and in microbial degradation of organic matter[46].

Although Fe(II)-oxidizers are present and active, they cannot prevent the overall loss of reactive Fe and Fe-associated OC along the palsa hillslope. The CO_2 produced from degradation of released carbon, including Fe-associated-OC, further stimulated methanogenic microorganisms at the collapsing front. This CO_2 production was at least partially driven by Fe(III) reduction coupled to carbon oxidation based on the increasing abundance of Fe(III)-reducing bacteria along the palsa hillslope as has also been suggested for subalpine wetland soils[47].

Ultimately, the loss of this so called rusty carbon sink contributes to net GHG emissions of CO_2 and CH_4, directly by Fe(III) reduction coupled to carbon oxidation and indirectly by promoting methanogenesis at the collapsing front.

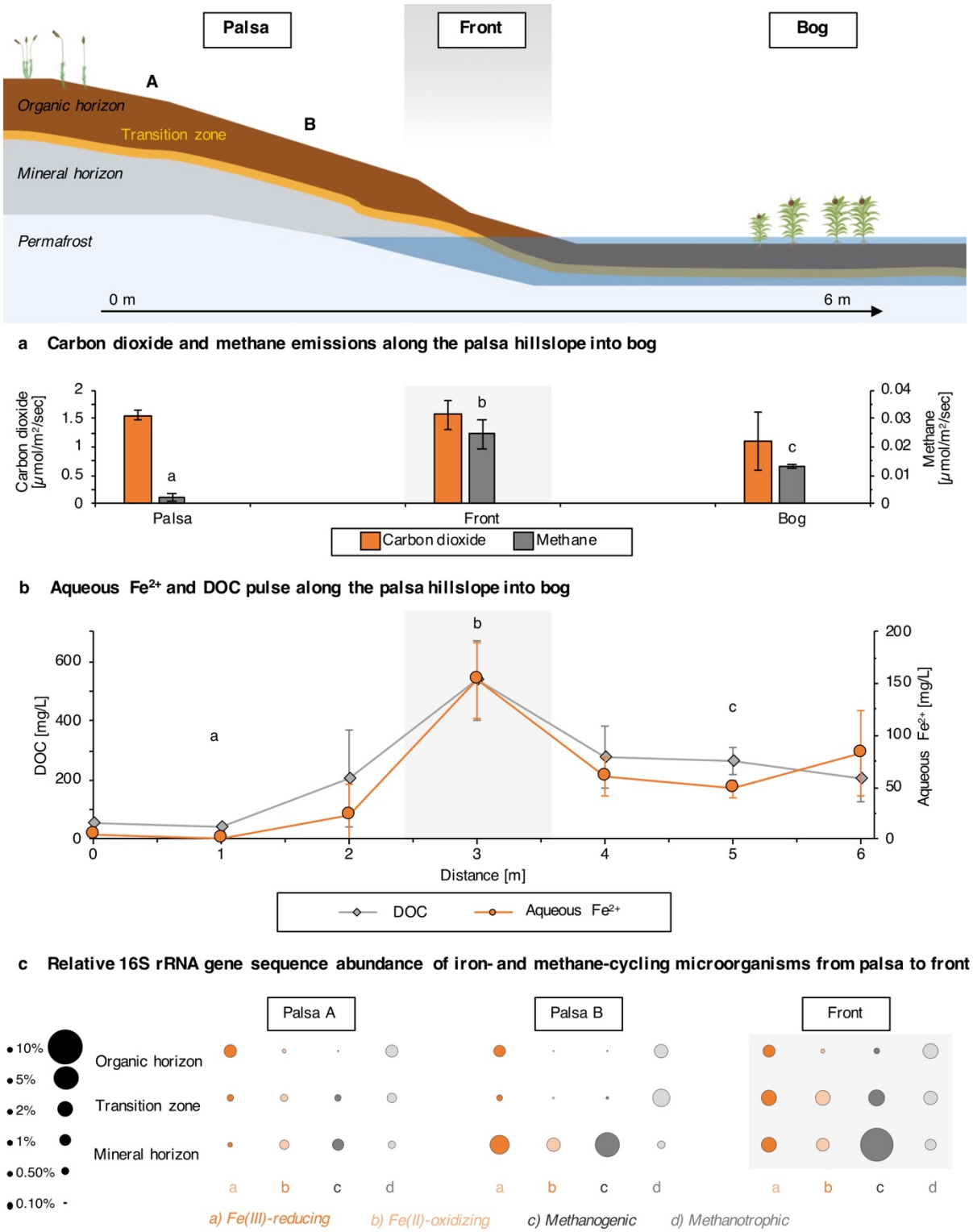

Figure 1. Microbial iron cycling and carbon release as dissolved organic carbon (DOC), carbon dioxide and methane emissions along a palsa hillslope. a, Carbon dioxide and methane emissions along the palsa hillslope with highest emissions at the collapsing front. The

reported values and error bars represent the average and standard deviation of measurements collected on three days at three separate time points. b, Aqueous iron (Fe^{2+}) and DOC pulse along the palsa hillslope at 30 cm depth with highest values at the collapsing front. Reported values and error bars represent the average and standard deviation of eight palsa to bog hillslopes sampled in June/July 2019 c, Relative 16S rRNA gene abundance of iron- and methane-cycling strains along the palsa hillslope with highest abundances at the collapsing front: a) Fe(II)-oxidizing, b) Fe(III)-reducing, c) methanogenic and d) methanotrophic. Small letters above data mean significant differences ($P<0.05$, one-way ANOVA: TukeyHSD test).

Microbial iron- and methane-cycling communities during palsa collapse. Along the palsa hillslope, iron- and methane-cycling microorganisms increase in relative abundance, here defined as DNA-based relative 16S rRNA gene abundance, and in potential activity, here defined as RNA-based relative 16S rRNA abundance (Figure 2; for total microbial community and replicate analysis see Figure S9 and S11, Table S1-S4).

Fe(III)-reducers, driving reactive Fe mineral dissolution and associated OC release, are found in high abundance and potential activity along the palsa hillslope. From Palsa A to the collapsing front, *Geobacter* spp., a classical Fe(III)-reducer[24], increased in relative abundance from 0 to 1.55±0.30% in the transition zone and to 1.62±0.18% in the mineral horizon. The potential activity of *Geobacter* spp. rose from 0 to 2.50±0.13% in the transition zone and to 4.75±1.07% in the mineral horizon (Figure 2). *Clostridium* spp., a fermentative Fe(III)-reducer[53], increased in relative abundance from 0 to 0.81±0.02% in the transition zone and 0.76±0.07% in the mineral horizon (Figure 2). Potential activity of *Clostridium* spp. increased from 0 to 2.31±1.15% in the transition zone and to 1.23±0.22% in the mineral horizon (Figure 2). *Rhodoferax* spp., known for dissimilatory Fe(III) reduction[52], only appeared to be present

(1.98±1.51%) and potentially active (1.62±0.16%) in the mineral horizon of the more collapsed palsa (Palsa B), close to the collapsing front (Figure 2). *Myxococcales* spp. showed highest relative abundance from 1.67±0.15% in the intact palsa (Palsa A) to 1.30±0.23% at the collapsing front and potential activity from 9.13±0.08 in the intact palsa to 7.03±2.08% at the collapsing front in the organic horizon (Figure 2).

This microbial community analysis further indicates that the rusty carbon sink is lost by dissimilatory and fermentative Fe(III) reduction. Dissimilatory Fe(III) reduction is conducted along the palsa hillslope by abundant and active Fe(III)-reducing microorganisms such as *Geobacter* spp., *Rhodoferax* spp. and *Myxococcales* spp. (Figure 2; see also absolute abundances in Figure S8 and replicate core analysis in Figure S15)[48,49]. *Myxococcales* spp. are not only capable of Fe(III) reduction, but also e.g. polysaccharide and protein degradation[46]. *Geobacter* spp. and *Rhodoferax* spp. represent classical Fe(III)-reducing microorganisms, that are well studied in different environments[23] with *Rhodoferax* spp. also being described at other permafrost sites[14]. Fermentative Fe(III) reduction is probably performed by *Clostridium* spp. who might use the present DOC as carbon and energy source.

The abundant and active Fe(III)-reducing bacteria are accompanied by less relatively abundant and probably less active Fe(II)-oxidizers. *Gallionella* spp. had a relative abundance of 0.82±1.16% in the present microbial community and 1.42±1.92% in the active community of the mineral horizon of the more collapsed palsa (Palsa B). *Sideroxydans* spp. increased in their relative abundance from below detection to 1.42±0.21% in the transition and to 1.08±0.34% in the mineral horizon. Other *Gallionellaceae*, besides *Gallionella* spp. and *Sideroxydans* spp., were equally distributed in their relative abundance along the palsa hillslope from 0.54±0.26% in the transition zone and 0.86±0.55% in the mineral horizon of the intact palsa (Palsa A) to 0.90±0.12% in the transition zone and 0.58±0.09% in the mineral horizon at the collapsing front. The activity of the other *Gallionellaceae* was probably highest at the collapsing front

with 0.53±0.24% in the transition zone and 0.35±0.07% in the mineral horizon. The classical Fe(II)-oxidizing bacteria[48,49] such as *Gallionella* spp. and *Sideroxydans* spp., observed to be present and potentially active in this system were already described in arctic ponds[50]. In this setting, these cannot sustain or reform the rusty carbon sink during palsa collapse (Figure 2).

The increasing relative 16S rRNA (gene) abundance (DNA- and RNA-based) of classical Fe(III)-reducing bacteria is accompanied by an increase in the relative abundance of methanogenic microorganisms, mainly *Methanobacterium* spp. These significantly increased in their relative abundance in the transition zones from 0.25±0.24% in the intact palsa (Palsa A) to 2.05±0.14% at the collapsing front. In the mineral horizon, they rose in their relative abundance from 1.15±1.22% in the intact palsa (Palsa A) to 10.07±2.84% at the collapsing front (Figure 2). Along the palsa hillslope, only a slight increase in potential activity of *Methanobacterium* spp. was observed in the transition zone from 0 to 0.14±0.05% and in the mineral horizon from 0 to 1.91±0.85% (Figure 2). Other methanogens belonging to *Bathyarchaeia* also increased in relative abundance along the palsa hillslope from 0.17±0.13% to 0.71±0.12% in the transition zone and from 0.25±0.18% to 1.45±0.24% in the mineral horizon. Methanotrophs, such as *Roseiarcus* spp. and other *Beijerinckiacaeae* (i.e. *Methylobacterium* spp. or *Methylocystis* spp.) had an equal relative abundance in the community present along the palsa hillslope (i.e. DNA-based) and had its highest potential activity in the palsa closest to the collapsing front (Palsa B; 12.55±0.30%).

Acetate, formed along the palsa hillslope and accounted for up to 61.70±42.56 mg C/L (10.33% of the total DOC) at the collapsing front (Figure 4). It is expected that this stimulates Fe(III) reduction coupled to acetate oxidation and leads to CO_2 formation by Fe(III)-reducing bacteria such as *Geobacter* spp., known to metabolize acetate[23]. The potential for reductive acetogenesis from CO_2 by *Bathyarchaeia* was previously suggested[51]. Our MetaCyc ontology predictions showed a high potential for acetoclastic methanogenesis (Figure S12), but contradictory to this,

235 we only saw a high relative abundance of hydrogenotrophic methanogens such as
236 *Methanobacterium* spp. This could be explained by the higher thermodynamic favorability of
237 Fe(III) reduction coupled to acetate oxidation as compared to acetoclastic methanogenesis. H_2
238 and CO_2, partially produced by fermentation and Fe(III) reduction by e.g. *Clostridium* spp., can
239 be used by hydrogenotrophic methanogens and lead to CH_4 emissions at the collapsing front.
240 The CH_4 is partially oxidized back to CO_2 by methanotrophs as shown by Perryman *et al*.[22] who
241 described highest methane oxidation rates for palsa at the transition between palsa and bog (here
242 referred to as the collapsing front).
243 Our data clearly shows a co-existence of microbial iron- and methane-cycling microbial
244 communities during palsa collapse, which ultimately cause GHG emissions and effect the
245 balance between CO_2 and CH_4 emissions even before complete permafrost thaw.

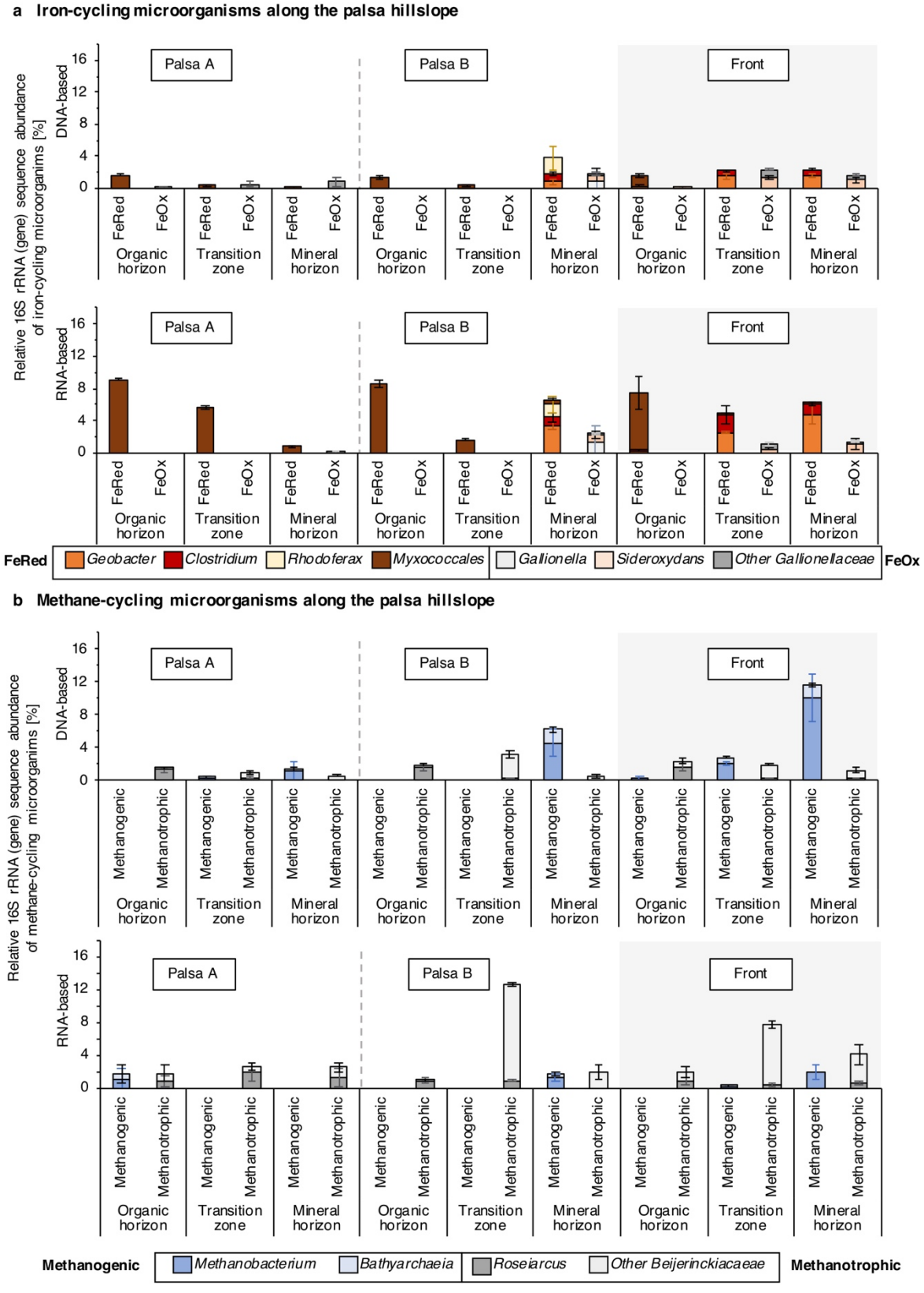

Figure 2. Relative 16S rRNA (gene) abundance of abundant (DNA-based) and likely active (RNA-based) iron (Fe)- and methane-cycling microbial communities along the palsa

hillslope (Palsa A, Palsa B, Front). a, Iron-cycling microorganisms show an increasing relative 16S rRNA (gene) abundance (DNA- and RNA-based) along the palsa hillslope with highest abundances in the transition zone and mineral horizon at the collapsing front. b, Methane-cycling microorganisms are increasing in relative 16S rRNA (gene) abundance along the palsa hillslope. Reported values and error bars represent the average and standard deviation of triplicate analysis of each soil horizon along the palsa hillslope. Replicate cores show similar relative 16S rRNA (gene) abundance of abundant (DNA-based) and potentially active (RNA-based) Fe- and methane cycling microbial communities along the palsa hillslope (Figure S11, Table S1-S4).

Release of bioavailable iron-associated organic carbon during palsa collapse. To investigate if the loss of the rusty carbon sink also directly contributes to net GHG emissions by releasing bioavailable, previously Fe-bound organic carbon, into the porewater we determined the quantity and identity of Fe-bound OC in the solid phase (defined as dithionite extractable OC) and of the released OC in the porewater. Dithionite did not affect the identity of extractable OC and did not lead to molecular artifact formation (see SI, Table S5).

Highest reactive Fe concentrations (defined as Fe reductively dissolved by sodium dithionite and control corrected by leachable Fe, see Methods) were found in the transition zone of the most intact palsa (10.04±0.07 mg reactive Fe per g soil; Figure 3). Towards the collapsing front, reactive Fe in the transition zone between the organic and mineral horizons significantly decreased to 3.22±0.06 mg per g soil at the front (Figure 3). Absolute values are listed in Table S6 and replicate core analysis can be seen in Figure S13. The amount of reactive Fe-associated OC (OC dissolved after reductive dissolution of reactive Fe minerals by sodium dithionite and control corrected by leachable OC, see Methods) also decreased from the palsa to the bog in

the transition zone (83.69±10.04 and 76.60±16.89 mg Fe-associated OC per g soil in the palsa to 40.88±10.76 mg per g soil in the bog) (Figure 2). In the organic horizons along the palsa hillslope, reactive Fe and Fe-associated OC abundance was the lowest in the soil profile with average values of 0.49±0.25 mg reactive Fe per g soil and 2.08±2.47 mg Fe-associated OC per g soil (Figure 3). In the mineral horizons from the palsa to the collapsing front, reactive Fe was very stable (average 3.81±0.38 reactive Fe per g soil), whereas Fe-associated OC slightly decreased from 47.21±14.30 mg Fe-associated OC per g soil in the palsa to the collapsing front which had only 11.60±8.54 mg Fe-associated OC per g soil (Figure 3). The highest content of Fe-associated OC was found in the most intact palsa along the palsa hillslope. This is supported by the strong spatial associations of OC with Fe minerals in the fine fraction observed by nanoSIMS analysis in the transition zone in this core (Figure 3; see replicate analysis of intact palsa core "Palsa A" in Figures S1, S14-S15). The transition zone and mineral horizons at the collapsing front showed organic-free, co-existing Fe and aluminum (Al), suggestive of Fe-bearing clays (Figure 3). This is also supported by Mössbauer spectroscopy (Figure S16, Table S7) and by previous observations with extended X-ray adsorption fine structure (EXAFS)[19].

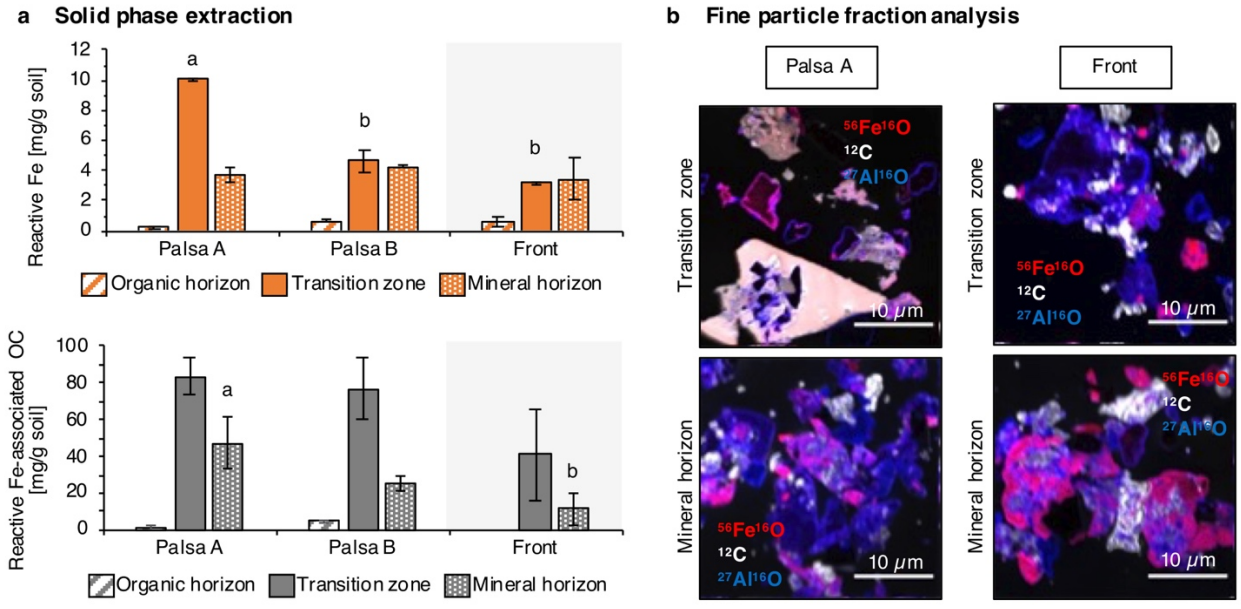

Figure 3. Reactive iron (Fe) and associated organic carbon (OC) from intact palsa to the collapsing front in a, the bulk soil and b, in the fine particle fraction. a, Reactive Fe and Fe-associated organic carbon in the solid phase decrease from the intact palsa (Palsa A) towards the collapsing front. Reactive Fe values are the average of sodium dithionite citrate duplicate extractions, control corrected by sodium chloride bicarbonate extractable Fe (leachable Fe). Fe-associated OC values are the average of sodium dithionite citrate extractions, control corrected by subtraction of the citrate background and the sodium chloride bicarbonate extractable OC (leachable OC) (see Methods). Error bars of reactive Fe represent a combined standard deviation of sodium chloride bicarbonate extractable Fe and sodium dithionite citrate extractable Fe. Errors of the Fe-associated carbon represent a combined standard deviation of the citrate blank, sodium chloride bicarbonate extractable OC and sodium dithionite citrate extractable OC. Different small letters above bars mean significant differences ($P<0.05$, one-way ANOVA: TukeyHSD test). b, High spatial resolution analysis of Fe-OC associations by nanoSIMS in the fine fraction of the soil, displayed as $^{12}C^-$ (white), $^{56}Fe^{16}O^-$ (red) and $^{27}Al^{16}O^-$ (blue) overlaid in a composite image. For the two end-members, Palsa A and collapsing front, four particles of the fine fractions of each layer were analyzed by correlative SEM and nanoSIMS, all showing the same spatial distribution of Fe, C and Al as shown by the four representatives (Figure S14-S15).

FT-ICR-MS analyses showed that, in the intact palsa, the reactive Fe-associated OC had a higher relative abundance of aliphatic species than the reactive Fe-associated OC at the collapsing front (Figure 4, un-processed van Krevelen diagrams in Figure S17). This more aliphatic-like fraction could represent amino sugar-like, carbohydrate-like and lignin-like compounds (O/C range: 0.3 to 0.6, H/C range: 1.0 to 1.5) [52,53]. A higher fraction of aromatics was associated with reactive Fe phases at the collapsing front compared to the organics bound

315 by reactive Fe in the intact palsa (Figure 4). In general, it should be noted that the amounts
316 (mg/g) of reactive Fe-associated OC are decreasing along the palsa hillslope (Figure 3 and Table
317 S5). The higher relative abundance of the more aliphatic compounds associated with reactive
318 Fe in the intact palsa is lost during reductive dissolution to the surrounding porewater along the
319 palsa hillslope, thus the aliphatic fraction most likely contributes to the aqueous Fe^{2+} and DOC
320 pulse at the collapsing front (Figure 4). Loosely bound OC (salt extractable) appeared in lower
321 quantities and showed less defined but similar identity of organic fractions to the reactive Fe-
322 associated OC (Figure S18, Table S5 and S7).

323 Porewater extracted from the same soil interface (transition zone), where the rusty carbon sink
324 is lost along the palsa hillslope (Figures 1 and 2), contained a higher relative abundance of more
325 aliphatic species and more aromatic species compared to porewater extracted at the collapsing
326 front (Figure 4; un-processed van Krevelen diagrams in Figure S17). At the collapsing front, an
327 increased relative abundance of organic molecules, potentially representing tannin-like
328 compounds (O/C range: 0.5 to 0.9, H/C range: 0.5 to 1.4)[52,53], is observed (Figure 4 ; Figure
329 S17). The more aliphatic species had a lower relative abundance in the DOC at the collapsing
330 front, whereas a higher relative abundance of more aromatic species was observed (Figure
331 4).This could indicate decomposition processes that occur in the palsa hillslope porewater that
332 yield smaller organic compounds, uptake by native microbes, assimilation of organic carbon
333 into biomass and/or further metabolism, and ultimately emissions of GHGs by microbial
334 respiration. Porewater analysis along a replicate palsa hillslope showed the same identity of
335 aliphatic and aromatic species in intact palsa and at the collapsing front (Figure S19).

336 Further decomposition of DOC along the palsa hillslope is supported by an increasing nominal
337 oxidation state of carbon (NOSC) of the DOC in the porewater at the transition zone from the
338 palsa towards the collapsing front from 0.12±0.04 to 0.24±0.04 (Figure 4). As the DOC
339 becomes more oxidized, the NOSC increases at the collapsing front. This is in line with an

increasing average molecular weight (MW) from 591.24±7.70 in palsa to 614.80± 0.40 at the collapsing front (Figure 4 b and Figure S20). NOSC values slightly decreased in the bog to 0.20±0.02 due to the overall loss of organic carbon mainly as CO_2 and, consequently, enrichment of less decomposed and more reduced DOC in the porewater. The double-bond equivalents (DBE, the number of rings plus double bonds to carbon, calculated from the neutral elemental composition[54]), remained stable along the palsa hillslope (0.39±0.08). The DBE along the palsa hillslope showed lower values than previously reported for bog and fen[44], indicating that bog and fen DOC is overall more unsaturated compared to DOC released along the palsa hillslope.

The further decomposition of released organic carbon contributes to acetate formation (Figure 4) at the collapsing front, probably by pyruvate fermentation, indicated by MetaCyc ontology predictions (Figure S12). Along the palsa hillslope, acetate in the porewater at the transition zone between organic and mineral horizons significantly increased (unpaired *t*-test, $N = 8$, $\alpha = 0.05$, $p = 0.0024$) from 6.24±0.34 mg C/L (3.56% of the total DOC) in the palsa to 61.70±42.56 mg C/L (10.33% of the total DOC) at the collapsing front, the highest acetate concentrations observed across the whole thaw gradient[19]. Further into the bog, the acetate concentrations significantly decreased from 15.13±6.53 to 6.10±1.44 mg C/L.

Previous studies at Stordalen mire focused on the soil organic carbon quantity and identity as well as on dissolved organic matter composition (DOM) and DOC transport along the thaw gradient. These analyses have highlighted shifts towards faster decomposition from partially-thawed bog to fully-thawed fen with an increasing proportion of carbon released as CH_4[40,44,55]. Processes occurring at the transition between palsa and bog had not been studied, thus enhanced production of acetate and its promotion of methanogenesis at this transition has been overlooked.

Our data showed that reactive Fe at the redox boundary between organic and mineral horizons can bind aliphatic organic carbon, probably by downward cycling of DOM (defined as continuous sorption and precipitation of DOM, as well as of microbial processing, desorption and dissolution proportions of more recent plant-derived compounds[56,57]) which is released during reductive dissolution into the surrounding porewater. Lower molecular weight compounds, aliphatic compounds or compounds poor in carboxyl functional groups show lower binding strength to Fe minerals than higher molecular weight compounds, aromatics, or compounds rich in carboxyl functionalities[57]. This is also supported by the leachable OC extractions (same ionic strength and pH as the sodium dithionite extraction; Figure S18). Thus, these compounds are not protected from microbial degradation along the palsa hillslope. The previously Fe-associated aliphatic fraction becomes more bioavailable to microorganisms when it is released from mineral associations[57]. This likely contributes to promotion of microbial growth and respiration of DOM during permafrost thaw[56,58-60]. Relative to aromatic compounds, aliphatic compounds are expected to be even more labile to microorganisms [56,59,60], which is supported by the overall loss of this more aliphatic carbon fraction in the porewater at the collapsing front (Figure 4) with only minor quantities of aromatic organic molecules remaining preserved by reactive Fe minerals after palsa collapse (Figure 3 and Figure 4). Kawahigashi *et al*. showed that aromatic DOC was preferentially retained by mineral horizons in Siberian tundra containing reactive Fe[35].

Our data clearly suggests that the loss of this rusty carbon sink directly contributes to high DOC concentrations along the palsa hillslope and provides a bioavailable organic carbon source that stimulates microbial respiration and promotes GHG emissions.

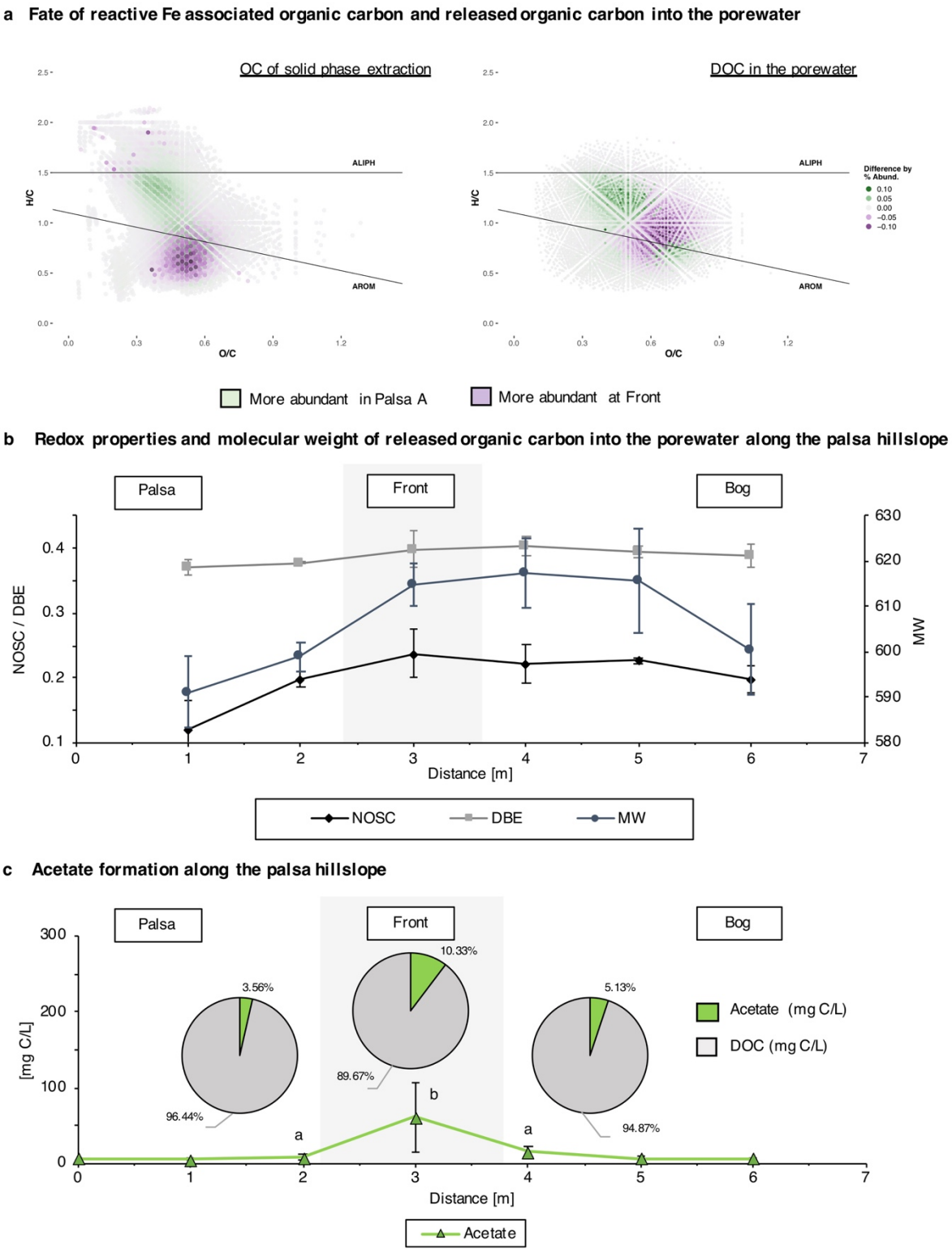

386

387 **Figure 4. Bioavailability of reactive iron (Fe)-associated organic carbon (OC) released**
388 **along the palsa hillslope.** a, Composition of reactive Fe-associated OC and OC released into
389 the porewater. Fe-bound carbon in palsa soils, underlain by intact permafrost, is comprised of

more aliphatic species (class 1, green) and more aromatic species (class 2, purple). This is lost with reductive dissolution into the porewater. Towards the collapsing front into the bog, the remaining Fe-associated OC fraction (purple) is comprised of less bioavailable organic compounds which are likely associated with clay minerals (common in Palsa A, Front and Bog). Dissolved OC, which is only found in Palsa A, is enriched in more aliphatic compounds (green). Towards Front and Bog, only more aromatic species (purple) remain (Figures S17-S19, Table S5). B, Redox properties and molecular weight of released organic carbon into the porewater along the palsa hillslope (Figure S20). Reported values and error bars represent the average and the range of duplicate porewater analysis along two palsa hillslopes (Figures S1 and Figure S4). a, Acetate formation along the palsa hillslope. Following further decomposition of the dissolved OC, highly bioavailable acetate [mg C/L] is formed which then is again used to further reduce present reactive Fe(III) to Fe^{2+} coupled to acetate oxidation and CO_2 formation. Reported values and error bars represent the average and standard deviation of 8 palsa to bog hillslopes, sampled in June/July 2019 (Figures S1 and Figure S4). Different small letters above data mean significant differences ($P<0.05$, one-way ANOVA: TukeyHSD test).

Implications for the carbon cycle in thawing permafrost peatlands. There is a substantial need to piece together carbon sources and sinks in thawing permafrost environments to better understand and quantitatively predict the overall climate impact of permafrost thaw[61]. One such carbon sink or source are Fe-OC associations[36], which sequesters organic carbon in intact permafrost soils[20] but releases it with complete permafrost thaw[19]. Our data now showed that the release of the OC from the rusty carbon sink turns the OC into a source of labile DOC, CO_2 and CH_4 even before permafrost-supported palsas have completely collapsed. With increasing abrupt thaw, occurring in 20% of the permafrost zone, new active hillslope features are formed[62] and thus could speed up the loss of the rusty carbon sink in currently intact permafrost

415 environments. Newest estimates showed that collapsing fronts will occupy 3% of abrupt thaw
416 terrain by 2300, but could emit one-third of abrupt thaw carbon losses[62]. Ultimately, interlinked
417 processes of iron- and carbon cycling in thawing permafrost environments need to be integrated
418 into existing climate models to better understand and predict GHG emissions of thawing
419 permafrost areas and thus better estimate its overall climate impact. For this, it is crucial to
420 further determine co-occurring Fe(III) reduction rates and CO_2 and CH_4 production rates
421 following Fe mineral dissolution.
422

METHODS

Site information. Stordalen Mire (68 22' N, 19 03' E) is a subarctic peatland in northern Sweden underlain by discontinuous permafrost. The mire consists of three distinct sub-habitats: (1) palsa (intact permafrost) with ericaceous and woody plants; (2) ombrotrophic peatland or bog (intermediate thaw) with *Sphagnum spp*., sedges and shrubs and (3) minerotrophic peatland or fen (fully thawed) with sedges, mainly *Eriophorum spp*[45] (Figure S1). Generally, palsas and bogs are only fed by precipitation and melt water and have more acidic surface waters (pH ~4). Fens are fed by surface water and groundwater, and maintain slightly acidic to alkaline pH[40]. The areal extent of intact palsa across Stordalen mire has declined significantly since 1970 due to progressive warming in the Arctic, while fen habitats have expanded[63]. It is also predicted that the whole mire might be free of permafrost as early as 2050[64,65].

Gas measurements. To measure CO_2 emissions along the palsa hillslope, two eosense instruments (eosFD Forced Diffusion chamber in conjunction with the eosLink-FD software, EOSENSE INC, Dartmouth, Canada) were installed (Figures S1 and S2): (1) at the top of the palsa hillslope (spot: Palsa A) and (2) at the transition to bog (spot: Front). The collar was situated in a flat location and inserted to near full depth. A centimeter of space was left to aid in installation of the eosFD itself as well as collar retrieval. The collar area was cleared of any rocks or debris, larger vegetation was removed or avoided. The eosFD was deployed in the installed collar. The collars were deployed at least 24 hours prior to the start of the eosFD measurement collection to avoid disturbance-related fluxes in the early portion of the data collection. The eosFD samples gases from the atmospheric and soil cavities within the device. Briefly, gas is pulled from the atmospheric cavity to the sensor for 20 seconds to purge the sensor cavity, then sampled every 10 minutes for five samples. Gas is then pulled from the soil cavity for 20 seconds, then pulsed every 10 minutes for five samples. Forced diffusion flux is calculated as follows:

448 $$\frac{V}{A} * \frac{\partial C}{\partial t} = Fs - D\left(\frac{\Delta C}{L}\right)$$

449 (volume/surface area scaled rate of change in flux rate equal to the flux from the soil surface
450 (Fs) minus the difference in concentration, ΔC (scaled by both the path length L and the
451 diffusivity of the interface (membrane), D)).

452 The change in the flux rate over the timespan of the concentration measurements (around 60
453 seconds) is assumed to be zero (steady state):

454 $$\frac{V}{A}\frac{\partial C}{\partial t} = 0$$

455 This assumption results in a linear dependence with the path length and interface (membrane)
456 diffusivity being constant and represented by a single coefficient, G:

457 $$Fs = G\,\Delta C$$

458 Furthermore, carbon dioxide and methane emissions along the palsa hillslope were measured
459 in triplicate using plastic chambers sealed with a rubber stopper (Figures S1 and S2), as
460 described previously[66]. The metal frames were pushed into the ground at least 24 hours before
461 the measurements to avoid collecting gas emissions from the soil during installation. Again
462 rocks, debris and larger vegetation was avoided. Deionized water was used in the frames to seal
463 off the chambers from ambient air. Gas chamber samples were collected with a gas-tight syringe
464 (1100TLL 100 mL Gastight, Hamilton, Reno, NV, USA) and directly transferred into evacuated
465 12 mL exetainer vials[67] until analyzed. The sampling was done every 5 min for a total period
466 of 30 mins in duplicates for palsa and front and in triplicates for bog. All gas samples from the
467 field and standard gases used for calibration were measured with a gas chromatograph (Hewlett
468 Packard, 5890 Series II) equipped with an electron capture detector (^{63}Ni-ECD).

Sample collection. In July 2019, cores were taken along three palsa hillslopes (Figure S1 and Figure S7), gently collapsing into bog, following the expected hydrological flow described previously[40]. A Humax corer of 50 cm length and 3-cm diameter with inner liners was used to sample the active layer[19]. The cores for mineral analysis were directly split after sampling under 100% N_2 atmosphere in a glove bag and subsamples stored at -20°C until analysis. The cores for microbial community analysis were split directly in the field, immediately frozen with liquid nitrogen and stored at -80°C until further processing. As previously described[19], the cores were split into three soil horizons based on texture and color changes: (1) A peat or organic horizon, followed by (2) a transition zone between the organic-rich and mineral-rich layer and (3) a mineral horizon.

In July and September 2019, porewater samples were collected from 30 and 60 cm depth below the peat surface along the palsa hillslope (8 transects, Figure S1 and Figure S4) using a luer lock syringe connected to a lysimeter with an effective pore size of 2.5 microns (Simpler Luer-Lock Micro Samplers, Model 1910LL, Soilmoisture Equipment Corp., Santa Barbara, CA). Prior to use, syringes and lysimeters were rinsed 10 times with 50 mL MiliQ water and air dried. Syringe filters (0.22 μm, PES, Merck™ Steritop™, Millipore) were pre-rinsed with 120 mL MilliQ water each to avoid leaching residuals of the filters. The syringes were flushed three times with N_2 and sealed till further use. Syringe filters (0.22 μm) were flushed three times with N_2 and placed into a SCHOTT bottle with N_2 atmosphere till further use. The lysimeters were installed in the soil, pre-flushed by pulling porewater with a syringe and the first 2 mL discharged. Immediately afterwards, the N_2 flushed syringes were unsealed, nitrogen gas pushed out, and then tightly connected to the installed lysimeter. To avoid direct sunlight exposure, syringes were covered with white cotton bags during the time of porewater extraction. After 3-4 hours, the samples were filtered through a 0.22 μm syringe filter into stoppered, N_2

493 flushed glass vials, wrapped in aluminum foil to avoid any sunlight exposure. The first 1 mL
494 filtrate from each sample was disposed. The samples were stored at 4°C till further analysis.

495 **Selective iron and carbon extractions.** To extract reactive Fe and associated OC, selective
496 dissolutions were conducted as described previously[19]. Briefly, a sodium bicarbonate (0.11 M)
497 sodium dithionite (0.27 M) trisodium citrate (0.27 M) solution was used to reductively dissolve
498 reactive Fe and associated organic carbon. As described in Lalonde *et al.*[11], a sodium
499 bicarbonate (0.11 M) sodium chloride (1.85 M) solution was used as a control experiment to
500 distinguish between Fe and OC readily desorbed (leachable OC) and organic carbon associated
501 with reactive Fe and only dissolved during reductive dissolution with dithionite. The citrate
502 background in the extract also needs to be subtracted to receive the reactive Fe-associated OC.
503 Thus, only the control corrected values are discussed:

504 $$Reactive\ Fe = Fe(dithionite\ citrate) - Fe(sodium\ chloride) \quad (1)$$

505 $$Reactive\ Fe - associated\ OC$$
506 $$= DOC(dithionite\ citrate) - DOC(blank\ citrate) - DOC(sodium\ chloride) \quad (2)$$

507 For each soil horizon (organic horizon, transition zone, mineral horizon), 0.3 g dry soil was
508 weighed into 10 mL glass vials with 6.25 mL extractant and N_2 headspace. After 16 hours at
509 room temperature on a rolling shaker, samples were centrifuged at room temperature for 10 min
510 at 5300 g. The supernatant was decanted and further analyzed for total Fe and DOC.

511 **Geochemical analysis.** To determine total Fe and Fe(II), porewater or extract was acidified in
512 1 M HCl and quantified spectrophotometrically in triplicates with the ferrozine assay[68]. DOC
513 was measured in triplicates with a total organic carbon analyzer (High TOC II, Elementar,
514 Elementar Analysensysteme GmbH, Germany). Inorganic carbon was removed by acidification
515 with 2 M HCl addition prior to analysis. High performance liquid chromatography (HPLC;
516 class VP with refractive index detector [RID] 10A and photo-diode array detector SPD-M10A

VP detectors; Shimadzu, Japan) was used to determine the fatty acid concentrations. To further quantify other elements in the porewater (i.e. phosphorous and sulfur) the samples were acidified in 1% (v/v) HNO_3 and analyzed in triplicates by inductively coupled plasma mass spectrometry (ICP-MS/MS Agilent 8900). A flow injection analysis (FIA) instrument equipped with a dialysis membrane for removal of Fe to prevent side reactions during measurement (Seal Analytical, Germany) was applied for quantification of NH_4^+, NO_3^- and NO_2^- concentrations.

Correlative SEM and nanoSIMS analysis. The free particles of the fine fraction of each organic horizon, transition zone and mineral horizon in cores Palsa A (referred to intact palsa), Palsa B (referred to more collapsed palsa) and Front (referred to collapsing front) along the palsa hillslope were analyzed using correlative SEM and nanoSIMS, as described previously[19,69,70]. Briefly, subsamples of each layer (1 mg) were dispersed in anoxic deionized water and gently shaken to obtain the free organo-mineral particles. All larger particles and aggregates were allowed to settle. A drop of 100 μl of the suspension was placed on a silica wafer and dried in an anoxic glovebox (N_2 atmosphere). Finally, samples were sputter-coated with ~30 nm Au/Pd conductive layer using a Bal-Tec SCD005 sputter coater (Baltec GmbH, Germany). To characterize the organo-mineral particles of the fine fraction by size and crystallinity and identify representative particles, a field emission scanning electron microscope (FE-SEM; Jeol JSM-6500F), equipped with secondary electron detector, was used prior to nanoSIMS analysis. The acceleration voltage was set to 5 kV, with a working distance of 10 mm. The nanoSIMS analysis were performed at the Cameca nanoSIMS 50L of the Chair of Soil Science (TU München, Germany). As described previously[19], a primary ion beam (~2 pA) was set at a lateral resolution ~100 nm and scanned over the samples with $^{12}C^-$, $^{16}O^-$, $^{12}C^{14}N^-$, $^{31}P^-$, $^{32}S^-$, $^{27}Al^{16}O^-$ and $^{56}Fe^{16}O^-$ secondary ions collected using electron multipliers.

Mössbauer spectroscopy. The soil samples for ^{57}Fe Mössbauer spectroscopy were collected under the protection of 100% N_2. Samples from three thaw stages were measured, including Palsa A, Bog and Fen (both wetland cores obtained by a previous campaign see Patzner *et al.*[19]) of transition zone and mineral horizon (Figure S16 and Table S7). The samples were dried anoxically before loading into a Plexiglass holder. The prepared samples were stored anoxically at -20°C until measurement. Mössbauer spectroscopy was performed in a standard transmission setup (Wissel, Wissenschaftliche Elektronik GmbH), and absorption spectra were collected at 77 and 6 K controlling with a closed-cycle cryostat (SHI-850-I, Janis Research Co). The spectra were calibrated with $\alpha^{57}Fe^0$ foil at 295 K, and fitted using the Voigt Based Fitting (VBF)[71] routine in the Recoil software (University of Ottawa, Canada). Results are shown in the Figure S16 and Table S7.

TOC and TN analysis. As described previously[19], total organic carbon (TOC) and total organic nitrogen (TN) were quantified by an Elementar vario El (Elementar Analaysysteme, GmbH, Germany). Soil samples were dried at 60°C until no further weight loss was observed. The dried soils were ground and acidified with 16% HCl to remove the inorganic carbon. After washing with deionized water, followed by drying, the TOC and TN content was analyzed. Results of C/N ratios are shown in the SI (Figure S10).

Microbial community analysis. Total RNA and DNA was extracted using the PowerSoil® RNA and DNA isolation kit as described by the manufacturer (MO BIO Laboratories, Carlsbad, CA, USA), with the following modifications: 2-3 g of soil was used from each soil horizon; 10 min bead-beating; centrifugation steps at maximal speed (7000 x g) at 4°C; and longer incubation times at -20°C (1.5 h). RNA and DNA were eluted in 50 μl RNase/DNase-Free water. RNA and DNA concentrations were determined using a Qubit® 2.0 Fluorometer with RNA and DNA HS kits (Life Technologies, Carlsbad, CA, USA). Subsequent DNA digestion

565 and reverse transcription reactions were performed using a Reverse Transcriptase (Invitrogen,
566 Life Technologies) as described previously by Otte *et al*., 2018[48]. Quantitative PCR (qPCR)
567 specific for the 16S rRNA (gene) of bacteria and archaea was performed as described
568 previously[48]. Microbial 16S rRNA (genes) were amplified using primers 515F and 806R[72].
569 Quality and quantity of the purified amplicons were determined using agarose gel
570 electrophoresis and Nanodrop (NanoDrop 1000, Thermo Scientific, Waltham, MA, USA).
571 Subsequent library preparation steps (Nextera, Illumina) and sequencing were performed by
572 Microsynth AG (Switzerland) using the 2 × 250 bp MiSeq Reagent Kit v2 on an Illumina MiSeq
573 sequencing system (Illumina, San Diego, CA, USA). From 10,112 to 396,483 (average
574 113,374) read pairs were generated per sample in three separate sequencing runs on the same
575 MiSeq machine, resulting in total in 8.6 million read pairs. Quality control, reconstruction of
576 16S rRNA (gene) sequences and taxonomic annotation was performed with nf-core/ampliseq
577 v1.1.2[73,74] with Nextflow v20.10.0[75] using containerized software with singularity v3.4.2[76]. Data
578 from the three sequencing runs were treated initially separately by the pipeline using the option
579 "mulipleSequencingRuns" and ASV tables were merged. Primers were trimmed, and
580 untrimmed sequences were discarded (< 25%, on average 7.7%) with Cutadapt v2.6[77]. Adapter
581 and primer-free sequences were imported into QIIME2 version 2019.10.0[78], processed with
582 DADA2 version 1.10.0[79] to eliminate PhiX contamination, trim reads (before the median
583 quality drops below 35, i.e. position 230 in forward reads and 174 in reverse reads), correct
584 errors, merge read pairs, and remove PCR chimeras; ultimately, in total 9,576 amplicon
585 sequencing variants (ASVs) were obtained across all samples. Alpha rarefaction curves were
586 produced with the QIIME2 diversity alpha-rarefaction plugin, which indicated that the richness
587 of the samples had been fully observed. A Naive Bayes classifier was fitted with 16S rRNA
588 (gene) sequences extracted with the PCR primer sequences from the QIIME compatible, 99%-
589 identity clustered SILVA v132 database[80]. ASVs were classified by taxon using the fitted

classifier[81]. 225 ASVs that classified as chloroplasts or mitochondria were removed, totalling to < 7% (average 0.6%) relative abundance per sample, and the remaining 9,351 ASVs had their abundances extracted by feature-table (https://github.com/qiime2/q2-feature-table).

Pathways, i.e. MetaCyc ontology predictions, were inferred with PICRUSt2 version 2.2.0-b (Phylogenetic Investigation of Communities by Reconstruction of Unobserved States)[82] and MinPath (Minimal set of Pathways)[83] using ASVs and their abundance counts. Inferring metabolic pathways from 16S rRNA amplicon sequencing data is certainly not as accurate as measuring genes by shotgun metagenomics, but it yields helpful approximations to support hypotheses driven by additional microbiological and biogeochemical analyses[82].

FT-ICR-MS analysis. Soil extracts and DOM in the porewater were analyzed with FT-ICR MS to identify and monitor compositional changes in the mineral-associated organic carbon fraction and the mobile, DOC fraction. All of the samples were prepared for FT-ICR-MS analysis by solid phase extraction (SPE) under N_2 atmosphere (glove bag) following the procedure described by Dittmar *et al.*, 2008[84] and Li *et al.*, 2016[85] with some modifications. In brief, 1 g, 3 mL Bond Elut PPL cartridges (part#12102148, Aglient Technologies, Santa Clara, CA, USA) were conditioned with 5 mL of HPLC grade methanol (Simga-Aldrich, Rehovot, Israel), followed by 5 mL of 0.01 M HCl. Each sample was acidified to pH ~2.5 and then loaded onto the SPE columns, loading volume was adjusted to load a total of 0.5 mg C based on the TOC content. After sample loading, the SPE cartridges were rinsed with 5 mL of 0.01 M HCl followed by drying with N_2 for 3-5 mins. Finally, the samples were eluted with 1 mL of HPLC grade methanol and stored in airtight amber sample vials wrapped in aluminum foil at 4°C. There was no additional dilution of the samples performed prior to analysis by negative ion electrospray ionization.

The samples were analyzed with a custom-built FT-ICR mass spectrometer, equipped with a 21T superconducting solenoid magnet and a modular software package for data acquisition (Predator)[86]. Sample solution was infused via a microelectrospray source[87] (50 μm i.d. fused silica emitter) at 500 nL/min by a syringe pump. Typical conditions for negative ion formation were: emitter voltage, -3.0 kV; S-lens RF level, 45%; and heated metal capillary temperature, 350 °C. Ions were initially accumulated in an external multipole ion guide (1-5 ms) and released *m/z*-dependently[88]. Ions were excited to *m/z*-dependent radius to maximize the dynamic range and number of observed mass spectral peaks (32-64%)[89], and excitation and detection were performed on the same pair of electrodes[90]. The dynamically harmonized ICR cell in the 21 T FT-ICR is operated with 6 V trapping potential[91,92]. Time-domain transients (100 time-domain acquisitions for all experiments) of 3.1 seconds were acquired with the Predator data station that handled excitation and detection only, initiated by a TTL trigger from the commercial Thermo data station[93]. Mass spectra were phase-corrected[94] and internally calibrated with 10-15 highly abundant homologous series that span the entire molecular weight distribution (~150 to 1300 m/z) based on the "walking" calibration method[95]. Experimentally measured masses were converted from the International Union of Pure and Applied Chemistry (IUPAC) mass scale to the Kendrick mass scale[96] for rapid identification of homologous series for each heteroatom class[97]. Peaks with signal to noise ratios greater than 6 times the noise at the baseline root-mean-square (rms) noise at *m/z* 500 were exported to custom software (PetroOrg©) for additional formula and elemental composition assignment[98]. All assigned formulas were part of a ≥3 peak carbon series and had less than ±0.3 ppm mass error. A LOD of 6 σ was considered sufficient to minimize ionization difference effects between samples, and therefore biasing by large numbers of low abundance peaks. To further identify macro compositional shifts, analysis of differences between samples was performed only on peaks with ≥20% difference in relative abundance. Additionally, modified aromaticity index (ModAI) was calculated according to

638 Koch&Dittmar[84] and nominal oxidation state of carbon (NOSC) was calculated according to La
639 Rowe&Van Cappellen[99]. Data processing post formula assignment was performed with
640 RStudio utilizing R software (V4.0.3).

641 **Statistical analysis.** The geochemical parameters were checked with the test of homogeneity.
642 Then a one-way analysis of variance (ANOVA) was used to identify differences in the
643 geochemical parameters along the palsa hillslope, combined with a post-hoc test to identify
644 significant differences between the different sampling spots along the palsa hillslope (from
645 palsa to collapsing front to bog). Based on Gloor *et al.*[100] no statistical analysis (such as e.g.
646 one-way ANOVA or unpaired t-test) were chosen for the compositional data obtained by 16S
647 rRNA Amplicon (gene) sequencing.

648

AUTHOR INFORMATION:

Corresponding author:

e-mail: casey.bryce@bristol.ac.uk

Author Contributions:

The original hypothesis was formulated by M.S.P., C.B. and A.K. M.S.P., C.B. and A.K. designed the project, interpreted the data and wrote the manuscript. M.S.P, C.B. and M.L. collected the samples. M.S.P. and M.L. gathered the data presented in the main text. A.M. conducted the FT-ICR-MS measurements and contributed to the data interpretation. T.B. and R.Y. contributed to the data analysis and interpretation. Z.Z. performed the Mössbauer spectroscopy and helped interpreting the results. H.J. helped collecting the porewater samples and data interpretation. C.H. and C.W.M., together with M.S.P., collected, analyzed and interpreted the nanoSIMS data. D.S. processed the amplicon sequencing data and, together with S.K., helped with interpretation of the microbial community results. T.S. contributed to project design and data interpretation. All authors contributed to the preparation of the manuscript and have given approval to the final version of the manuscript.

Notes:

The authors declare no competing interests.

ACKNOWLEDGEMENTS:

We are grateful for assistance in field work and sampling by Sara Anthony and the Arctic Research station (Abisko Sweden), especially thankful to Jennie Wikström, Eric Lundin, Niklas Rakos and Alexander Meire. We are thankful to Mette Svenning (Arctic University of Norway, Tromsø, Norway) for providing the gas chambers with the plastic lids. We thank EOSENSE INC, Dartmouth, Canada for getting the chance to use the EOSENSE gas chambers for our

672 research. We thank Sara Anthony for analysis of gas samples, Miroslava Malusova and Katrin
673 Wunsch for assistance in the lab, Timm Bayer for his help during SEM analysis and Johann
674 Lugmeier for assistance during nanoSIMS analysis. The authors acknowledge infrastructural
675 support by the Deutsche Forschungsgemeinschaft (DFG, German Research Foundation) under
676 Germany's Excellence Strategy, cluster of Excellence EXC2124, project ID 390838134. This
677 work was supported by the University of Tuebingen (Programme for the Promotion of Junior
678 Researchers award to Casey Bryce) and by the German Academic Scholarship Foundation
679 (scholarship to Monique Patzner). Sara Kleindienst is funded by an Emmy-Noether fellowship
680 from the DFG (grant number 326028733). Daniel Straub was funded by the Institutional
681 Strategy of the University of Tuebingen (DFG, ZUK63). The National High Magnetic Field
682 Laboratory is supported by the National Science Foundation Divisions of Chemistry and
683 Materials Research through DMR-1644779, Florida State University, and the State of Florida.
684

685 REFERENCES:

686 1 Ping, C. L., Jastrow, J. D., Jorgenson, M. T., Michaelson, G. J., Shur, Y. L. Permafrost
687 soils and carbon cycling *Soil* **1**, 147-171 (2015).
688 2 Schuur, E. A. G. *et al*. Climate change and the permafrost carbon feedback. *Nature* **520**,
689 171-179 (2015).
690 3 Hugelius, G. *et al*. Estimated stocks of circumpolar permafrost carbon with quantified
691 uncertainty ranges identified data gaps. *Biogeosciences* **11**, 6573-6593 (2014).

692 4 Nowinski, N., Taneva, L., Trumbore, S., Welker, J. Decomposition of old organic
693 matter as a result of deeper active layers in a snow depth manipulation experiment.
694 *Oecologia* **163**, 785-792 (2010).

695 5 Vonk, J. E., Mann, P. J., Davydov, S., Davydova, A., Spencer, R. G. M., Schade, J.
696 High biolability of ancient permafrost carbon upon thaw. *Geophys Res Lett* **40**, 2689-
697 2693 (2013).
698 6 Henkner, J., Scholten, T., Kühn, P. Soil organic carbon stocks in permafrost-affected
699 soils in West Greenland. *Geoderma* **282**, 147-159 (2016).
700 7 Hemingway, J. D., Rothman, D.H., Grant, K.E., Rosengard, S.Z., Eglinton, T.I., Derry,
701 L.A., Galy, V.V. Mineral protection regulates long-term global preservation of natural
702 organic carbon. *Nature* **570**, 228-231 (2019).
703 8 Kleber, M., Mikutta, R., Torn, M. S., Jahn, R. Poorly crystalline mineral phases protect
704 organic matter in acid subsoil horizons. *Eur J Soil Sci* **56**, 717-725 (2005).
705 9 Baldock, J. A., Skjemstad, J.O. Role of soil matrix and minerals in protecting natural
706 organic materials against biological attack. *Org Geochem* **31**, 697-710 (2000).
707 10 Kleber, M. *et al*. Mineral-Organic Associations: Formation, Properties, and Relevance
708 in Soil Environments. *Adv Agron* **130**, 1-140 (2015).
709 11 Lalonde, K., Mucci, A., Ouellet, A., Gelinas, Y. Preservation of organic matter in
710 sediments promoted by iron. *Nature* **483**, 198-200 (2012).
711 12 Wagai, R., Mayer, L. M., Kitayama, K., Shirato, Y. Association of organic matter with
712 iron and aluminum across a range of soils determined via selective dissolution
713 techniques coupled with dissolved nitrogen analysis. *Biogeochemistry* **112**, 95-109
714 (2013).

13 Kogel-Knabner, I. *et al*. Organo-mineral associations in temperate soils: Integrating biology, mineralogy, and organic matter chemistry. *J Plant Nutr Soil Sc* **171**, 61-82 (2008).

14 Lipson, D. A., Jha, M., Raab, T. K., Oechel, W. C. Reduction of iron (III) and humic substances plays a major role in anaerobic respiration in an Arctic peat soil. *J Geophys Res-Biogeo* **115**, G00I06 (2010).

15 Lovely, D. R., Phillips, E. J. Novel mode of microbial energy metabolism: organic carbon oxidation coupled to dissimiliatory reduction of iron or mangenese. *Appl Environl Microbiol* **57**, 1536-1540 (1988).

16 Asano, M. & Wagai, R. Evidence of aggregate hierarchy at micro- to submicron scales in an allophanic Andisol. *Geoderma* **216**, 62-74005 (2014).

17 Totsche, K. U. *et al*. Microaggregates in soils. *J Plant Nutr Soil Sc* **181**, 104-136 (2018).

18 Coward, E. K., Thompson, A. T. & Plante, A. F. Iron-mediated mineralogical control of organic matter accumulation in tropical soils. *Geoderma* **306**, 206-216 (2017).

19 Patzner, M. S. *et al*. Iron mineral dissolution releases iron and associated organic carbon during permafrost thaw. *Nat Commun* **11,** 6329 (2020).

20 Mu, C. C. *et al*. Soil organic carbon stabilization by iron in permafrost regions of the Qinghai-Tibet Plateau. *Geophys Res Lett* **43**, 10286-10294 (2016).

21 Shelef, E., Rowland, J.C., Wilson, C.J., Hilley, G.E., Mishra, U., Altmann, G.L., Ping, C.L. Large uncertainity in permafrost carbon stocks due to hillslope soil deposits. *Geophys Res Lett* **44**, 6134-6144 (2017).

22 Perryman, C. K. M. *et al*. Thaw Transitions and Redox Conditions Drive Methane Oxidation in a Permafrost Peatland. *J Geophys Res-Biogeo* **125** (2020).

23 Kappler, A., Bryce, C., Mansor, M., Lueder, U., Byrne, J.M., Swanner, E. An evolving view on biogeochemical cycling of iron. *Nat Rev Microbiol* (2021).

24 Van Bodegom, P. M., Scholten, J. C. M.; Stams, A. J. M. Stams. Direct inhibition of methanogenesis by ferric iron. *FEMS Microbiol Ecol* **49**, 261-268 (2004).

25 Wagner, R., Zona, D., Oechel, W., Lipson, D. Microbial community structure and soil pH correspond to methane production in Arctic Alaska soils. *Method Enzymol* **19**, 3398-3410 (2017).

26 Baldock, J. A. & Skjemstad, J. O. Role of the soil matrix and minerals in protecting natural organic materials against biological attack. *Org Geochem* **31**, 697-7102000).

27 Christensen, B. T. Physical fractionation of soil and structural and functional complexity in organic matter turnover. *Eur J Soil Sci* **52**, 345-353 (2001).

28 Sanderman, J., Maddern, T., Baldock, J. Similar composition but differential stability of mineral retained organic matter across four classes of clay minerals. *Biogeochemistry* **121**, 409-424 (2014).

29 Six, J. *et al*. Sources and composition of soil organic matter fractions between and within soil aggregates. *Eur J Soil Sci* **52**, 607-618 (2001).

30 Daugherty, E. E. *et al*. Hydrogeomorphic controls on soil carbon composition in two classes of subalpine wetlands. *Biogeochemistry* **145**, 161-175 (2019).

31 Crump, B., Kling, G., Bahr, M., Hobbie, J. Bacterioplankton community shifts in arctic lake corrleate with seasonal changes in organic matter sources. *Appl Environ Microbiol* **69**, 2253-2268 (2003).

32 Judd, K. E., Crump, B.C., Kling, G.W. Variation in dissolved organic matter controls bacterial production and community composition. *Ecology* **87**, 2068-2079 (2006).

33 Zhao, Q. *et al*. Iron-bound organic carbon in forest soils: quantification and characterization. *Biogeosciences* **13**, 4777-4788 (2016).

34 Adhikari, D. & Yang, Y. Selective stabilization of aliphatic organic carbon by iron oxide. *Sci Rep-Uk* **5**, 11214 (2015).

35 Kawahigashi, M., Kaiser, K., Rodionov, A., Guggenberger, G. Sorption of dissolved organic matter by mineral soils of the Siberian forest tundra. *Global Change Biol* **12**, 1868-1877 (2006).

36 Eglinton, T. I. GEOCHEMISTRY A rusty carbon sink. *Nature* **483**, 165-166 (2012).

37 McCalley, C. K. *et al*. Methane dynamics regulated by microbial community response to permafrost thaw. *Nature* **514**, 478-481 (2014).

38 Mondav, R. *et al*. Discovery of a novel methanogen prevalent in thawing permafrost. *Nat Commun* **5**, 3212 (2014).

39 Singelton, C. M *et al*. Methanotrophy across a natural permafrost thaw environment. *The ISME Journal* **12**, 2544-2558 (2018).

40 Olefeldt, D. & Roulet, N. T. Effects of permafrost and hydrology on the composition and transport of dissolved organic carbon in a subarctic peatland complex. *J Geophys Res-Biogeo* **117**, G01005 (2012).

41 Tang, J. *et al*. Drivers of dissolved organic carbon export in a subarctic catchment: Importance of microbial decomposition, sorption-desorption, peatland and lateral flow *Sci Total Environ* **622-623**, 260-274 (2018).

42 Lynch, L. M. *et al*. Dissolved organic matter chemistry and transport along an Arctic tundra hillslope. *Global Biogeochem Cy* **33**, 47-62 (2019).

43 Lipson, D. A., Raab, T.K., Goria, D., Zlamal, J. The contribution of Fe(III) and humic acid reduction to ecosystem respiration in drained thaw lake basins of the Arcitc Coastal Plain. *Global Biogeochem Cy* **27**, 399-409 (2013).

44 Hodgkins, S. B. *et al*. Changes in peat chemistry associated with permafrost thaw increase greenhouse gas production. *P Natl Acad Sci USA* **111**, 5819-5824 (2014).

45 Johansson, T. *et al*. Decadal vegetation changes in a northern peatland, greenhouse gas fluxes and net radiative forcing. *Global Change Biol* **12**, 2352-2369 (2006).

46 Woodcroft, B. J. *et al*. Genome-centric view of carbon processing in thawing permafrost. *Nature* **560**, 49-54 (2018).

47 Pallud, C., Rhoades, C. C., Schneider, L., Dwivedi, P., Borch, T. Temperature-induced iron (III) reduction results in decreased dissolved organic carbon export in subalpine wetland soils, Colorado, USA. *Geochim Cosmochim Ac* **280**, 148-160 (2020).

48 Otte, J. M. *et al*. The distribution of active iron-cycling bacteria in marine and freshwater sediments is decoupled from geochemical gradients. *Method Enzymol* **20**, 2483-2499 (2018).

49 Weber, K. A., Achenbach, L. A., Coates, J. D. Microorganisms pumping iron: anaerobic microbial iron oxidation and reduction. *Nat Rev Microbiol* **4**, 752-764 (2006).

50 Emerson, D., Scott, J. J., Benes, J., Bowden, W. B. Microbial iron oxidation in the Arctic tundra and its implications for biogeochemical cycling. *Appl Environ Microbiol* **81**, 8066-8075 (2015).

51 Loh, H. Q., Hervé, V., Brune, A. Metabolic potential for reductive acetogenesis and a novel energy-converting [NiFe] Hydrogenase in Bathyarchaeia from termite guts - a genome-centric analysis. *Front Microbiol* **11,** 635786 (2021).

52 Tfaily, M. M.. Advanced solvent based methods for molecular characterization of soil organic matter by high-resolution mass spectrometry. *Anal Chem* **87**, 5026-5215 (2015).

53 Tfaily, M. M. *et al*. Sequential extraction protocol for organic matter from soils and sediments using high resolution mass spectrometry. *Anal. Chim. Acta* **972**, 54-61 (2017).

54 McLafferty, F. W., Choi, J., Tureček, F. & Turecek, F. Interpretation Of Mass Spectra. University Science Books, ISBN 0-935702-25-3 (1993).

55 AminiTabrizi, R. *et al*. Controls on soil organic matter degradation and subsequent greenhouse gas emissions across a permafrost thaw gradient in Northern Sweden. *Frontiers in Earth Science* **8**, 557961 (2020).

56 Ward, P. C., Cory, R. M. Chemical composition of dissolved organic matter draining permafrost soils. *Geochim Cosmochim Ac* **167**, 63-67 (2015).

57 Kaiser, K., Kalbitz, K. Cycling downwards - dissolved organic matter in soils. *Soil Biol Biochem* **52**, 29-32 (2012).

58 Fuchs, G., Boll, M., Heider, J. Microbial degradation of aromatic compounds - From one strategy to four. *Nat Rev Microbiol* **9**, 803-816 (2011).

59 Abbott, B. W., Larouche, J. R., Jones, J. B., Bowden, W. B., Balser, A. W. Elevated dissolved organic carbon biodegradability from thawing and collapsing permafrost. *J Geophys Res* **119**, 2049-2063 (2014).

60 Mann, P. J., Davydova, A., Zimov, N., Spencer, R.G.M., Davydov, S., Bulygina, E., Zimov, S., Holmes, R.M. Controls on the composition and lability of dissolved organic matter in Siberia's Kolyma River basin. *J Geophys Res* **117** (2012).

61 When permafrost thaws. *Nat Geosci* **13**, 765 (2020).

62 Turetsky, M. R. *et al*. Carbon release through abrupt permafrost thaw. *Nat Geosci* **13**, 138-143 (2020).

63 Malmer, N., Johansson, T., Olsrud, M., Christensen, T. R. Vegetation, climatic changes and net carbon sequestration in a North-Scandinavian subarctic mire over 30 years. *Global Change Biol* **11**, 1895-1909 (2005).

64 Fronzek, S., Carter, T. R., Raisanen, J., Ruokolainen, L., Luoto, M. Applying probabilistic projections of climate change with impact models: a case study for sub-arctic palsa mires in Fennoscandia. *Climatic Change* **99**, 515-534 (2010).

65 Parviainen, M., Luoto, M. Climate envelopes of mire complex types in Fennoscandia. *Geogr Ann A* **89a**, 137-151 (2007).

66 Liebner, S. *et al*. Shifts in methanogenic community composition and methane fluxes along the degradation of discontinuous permafrost. *Front Microbiol* **6**, 356 (2015).

67 Glatzel, S., Well, R. Evaluation of septum-capped vials for storage of gas samples during air transport. *Environ Monit Assess* **136**, 307-311 (2008).

68 Stookey, L. L. Ferrozine - a New Spectrophotometric Reagent for Iron. *Anal Chem* **42**, 779-781 (1970).

69 Kopittke, P. M. *et al*. Nitrogen-rich microbial products provide new organo-mineral associations for the stabilization of soil organic matter. *Global Change Biol* **24**, 1762-1770 (2018).

70 Keiluweit, M. *et al*. Nano-scale investigation of the association of microbial nitrogen residues with iron (hydr)oxides in a forest soil O-horizon. *Geochim Cosmochim Ac* **95**, 213-226 (2012).

71 Rancourt, D. G., Ping, J.Y. Voigt-based methods for arbitrary-shape static hyperfine parameter distributions in Mössbauer spectroscopy. *Nucl Instrum Methods Phys Res Sect B* **58**, 85-97 (1991).

72 Caporaso, J. G. *et al*. QIIME allows analysis of high-throughput community sequencing data. *Nat Methods* **7**, 335-336 (2010).

73 Ewels, P. A. *et al*. The nf-core framework for community-curated bioinformatics pipelines. *Nat Biotechnol* **38**, 276-278 (2020).

74 Straub, D. *et al*. Interpretations of environmental microbial community studies are biased by the selected 16S rRNA (gene) amplicon sequencing pipeline. *Front Microbiol* **11**, 550420 (2020).

75 Di Tommaso, P. *et al*. Nextflow enables reproducible computational workflows. *Nat Biotechnol* **35**, 316-319 (2017).

76 Kurtzer, G. M., Sochat, V., Bauer, M. W. Singularity: Scientific containers for mobility of compute. *PLoS One* **12**, e0177459 (2017).

77 Martin, M. Cutadapt removes adapter sequences from high-throughput sequencing reads. *EMBnet journal* **17**, 3 (2011).

78 Bolyen, E. *et al*. Reproducible, interactive, scalable and extensible microbiome data science using QIIME 2. *Nat Biotechnol* **37**, 852-857 (2019).

79 Callahan, B. J. *et al*. DADA2: High-resolution sample inference from Illumina amplicon data. *Nat Methods* **13**, 581-583 (2016).

80 Pruesse, E. *et al*. SILVA: a comprehensive online resource for quality checked and aligned ribosomal RNA sequence data compatible with ARB. *Nucleic Acids Res* **35**, 7188-7196 (2007).

81 Bokulich, N. A. *et al*. Optimizing taxonomic classification of marker-gene amplicon sequences with QIIME 2's q2-feature-classifier plugin. *Microbiome* **6**, 90 (2018).

82 Langille, M. G. I. *et al*. Predictive functional profiling of microbial communities using 16S rRNA marker gene sequences. *Nat Biotechnol* **31**, 814-821 (2013).

83 Ye, Y., Doak, T.G. A Parsimony Approach to Biological Pathway Reconstruction/Inference for Genomes and Metagenomes. *PLoS Comput. Biol.* **5**, e1000465 (2009).

84 Dittmar, T., Koch, B., Hertkorn, N., Kattner, G. A simple and efficient method for the solid-phase extraction of dissolved organic matter (SPE-DOM) from seawater. *Limnol Oceanogr-Meth* **6**, 230-235 (2008).

85 Li, Y. *et al*. Proposed Guidelines for Solid Phase Extraction of Suwannee River Dissolved Organic Matter. *Anal Chem* **88**, 6680-6688 (2016).

86 Blakney, G. T., Hendrickson, C. L., Marshall, A. G. Predator data station: A fast data acquisition system for advanced FT-ICR MS experiments. *Int J Mass Spectrom* **306**, 246-252 (2011).

87 Emmett, M. R., White, F. M., Hendrickson, C. L., Shi, S. D.-H., Marshall, A. G. Application of micro-electrospray liquid chromatography techniques to FT-ICR MS to enable high-sensitivity biological analysis. *J Am Soc Mass Spectrom* **9**, 333-340 (1998).

88 Kaiser, N. K., Savory, J. J., Hendrickson, C. L. Controlled ion ejection from an external trap for extended *m/z* range in FT-ICR mass spectrometry. *J Am Soc Mass Spectrom* **25**, 943-949 (2014).

89 Kaiser, N. K., McKenna, A. M., Savory, J. J., Hendrickson, C. L., Marshall, A. G. Tailored ion radius distribution for increased dynamic range in FT-ICR mass analysis of complex mixtures. *Anal Chem* **85**, 265-272 (2013).

90 Chen, T., Beu, S. C., Kaiser, N. K., Hendrickson, C. L. Note: Optimized circuit for excitation and detection with one pair of electrodes for improved Fourier transform ion cyclotron resonance mass spectrometry. *Rev Sci Instrum* **85**, 066107 (2014).

91 Boldin, I. A. & Nikolaev, E. N. Fourier transform ion cyclotron resonance cell with dynamic harmonization of the electric field in the whole volume by shaping of the excitation and detection electrode assembly. *Rapid Commun Mass Spectrom* **25**, 122-126 (2011).

92 Kaiser, N. K., Quinn, J. P., Blakney, G. T., Hendrickson, C. L., Marshall, A. G. A Novel 9.4 Tesla FT ICR mass spectrometer with improved sensitivity, mass resolution, and mass range. *J Am Soc Mass Spectrom* **22**, 1343-1351 (2011).

93 Blakney, G. T., Hendrickson, C. L., Marshall, A. G. Predator data station: A fast data acquisition system for advanced FT-ICR MS experiments. *Int J Mass Spectrom* **306**, 246-252 (2011).

94 Xian, F., Hendrickson, C. L., Blakney, G. T., Beu, S. C. & Marshall, A. G. Automated Broadband Phase Correction of Fourier Transform Ion Cyclotron Resonance Mass Spectra. *Anal Chem* **82**, 8807-8812 (2010).

95 Savory, J. J. *et al*. Parts-Per-Billion Fourier transform ion cyclotron resonance mass measurement accuracy with a "Walking" calibration equation. *Anal Chem* **83**, 1732-1736 (2011).

96 Kendrick, E. A mass scale based on CH_2 = 14.0000 for high resolution mass spectrometry of organic compounds. *Anal Chem* **35**, 2146-2154 (1963).

97 Hughey, C. A., Hendrickson, C. L., Rodgers, R. P., Marshall, A. G., Qian, K. N. Kendrick mass defect spectrum: A compact visual analysis for ultrahigh-resolution broadband mass spectra. *Anal Chem* **73**, 4676-4681 (2001).

98 Corilo, Y. E. The Florida State University: Tallahassee, Fl, USA. *PetroOrg* (2012).

99 LaRowe, D. E. & Van Cappellen, P. Degradation of natural organic matter: A thermodynamic analysis. *Geochim Cosmochim Ac* **75**, 2030-2042 (2011).

100 Gloor, G. B., Macklaim, J. M., Pawlowsky-Glahn, V., Egozcue, J. J. Microbiome Datasets are compositional: and this is not optional *Front Microbiol* **8**, 2224 (2017).

Supplementary Information for

Microbial iron(III) reduction during palsa collapse promotes greenhouse gas emissions before complete permafrost thaw

Monique S. Patzner[1], Merritt Logan[2], Amy M. McKenna[3], Robert B. Young[2], Zhe Zhou[1,4], Hanna Joss[1], Carsten W. Mueller[5,6], Carmen Hoeschen[5], Thomas Scholten[7], Daniel Straub[8,9], Sara Kleindienst[8], Thomas Borch[2], Andreas Kappler[1,11] & Casey Bryce[1,12]*

[1]Geomicrobiology, Center for Applied Geosciences, University of Tuebingen, Schnarrenbergstrasse 94-96, 72076 Tuebingen, Germany.

[2]Department of Soil & Crop Sciences and Department of Chemistry, Colorado State University, 307 University Ave, 80523-1170 Fort Collins, US.

[3] National High Magnetic Field Laboratory, Florida State University, Tallahassee, FL 32310-4005, US.

[4]Alfred-Wegener-Institute, Helmholtz Centre for Polar and Marine Research, Am Handelshafen 12, 27570 Bremerhaven, Germany

[5]Chair of Soil Science, TUM School of Life Sciences, Technical University of Munich, Emil-Ramann Strasse 2, 85354 Freising, Germany.

[6]Department of Geosciences and Natural Resource Management, University of Copenhagen, Øster Voldgade 10, 1350 Copenhagen, Denmark.

[7]Chair of Soil Science and Geomorphology, Rümelinstraße 19-23, 72070 Tübingen, University of Tuebingen, Germany.

[8]Microbial Ecology, Center for Applied Geosciences, University Tuebingen, Schnarrenbergstrasse 94-96, 72076 Tuebingen, Germany.

[9]Quantitative Biology Center (QBiC), University Tuebingen, Auf der Morgenstelle 10, 72076 Tuebingen, Germany.

[11] Cluster of Excellence: EXC 2124: Controlling Microbes to Fight Infection, Tübingen, Germany.

[12]School of Earth Sciences, University of Bristol, Wills Memorial Building, Queens Road Bristol BS8 1RJ, UK.

*Corresponding Author: Casey Bryce

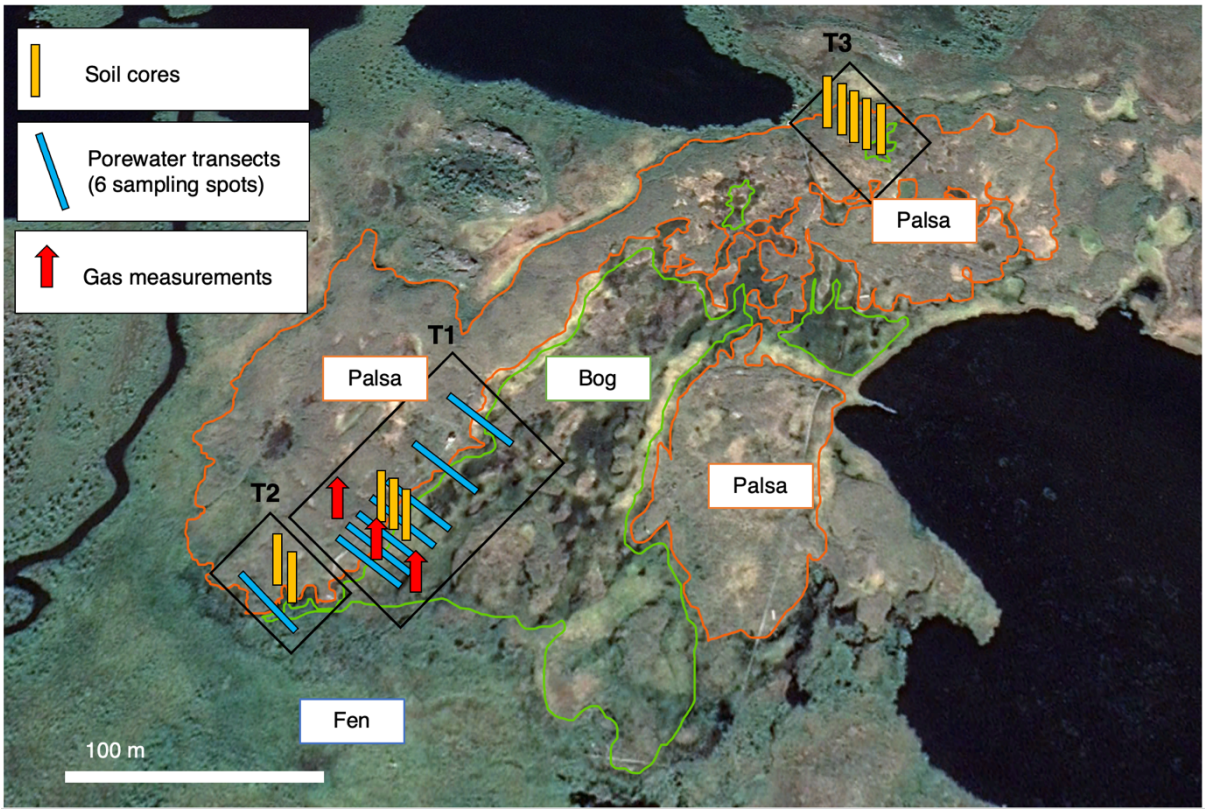

Figure S1. Field site and sample collection. Soil cores (yellow), porewater samples (blue) and gas samples (red) were taken in three transects (T1, T2 and T3) along palsa hillslopes into bog at Stordalen mire, Abisko (Sweden). Background picture was taken by GoogleEarth in 2019.

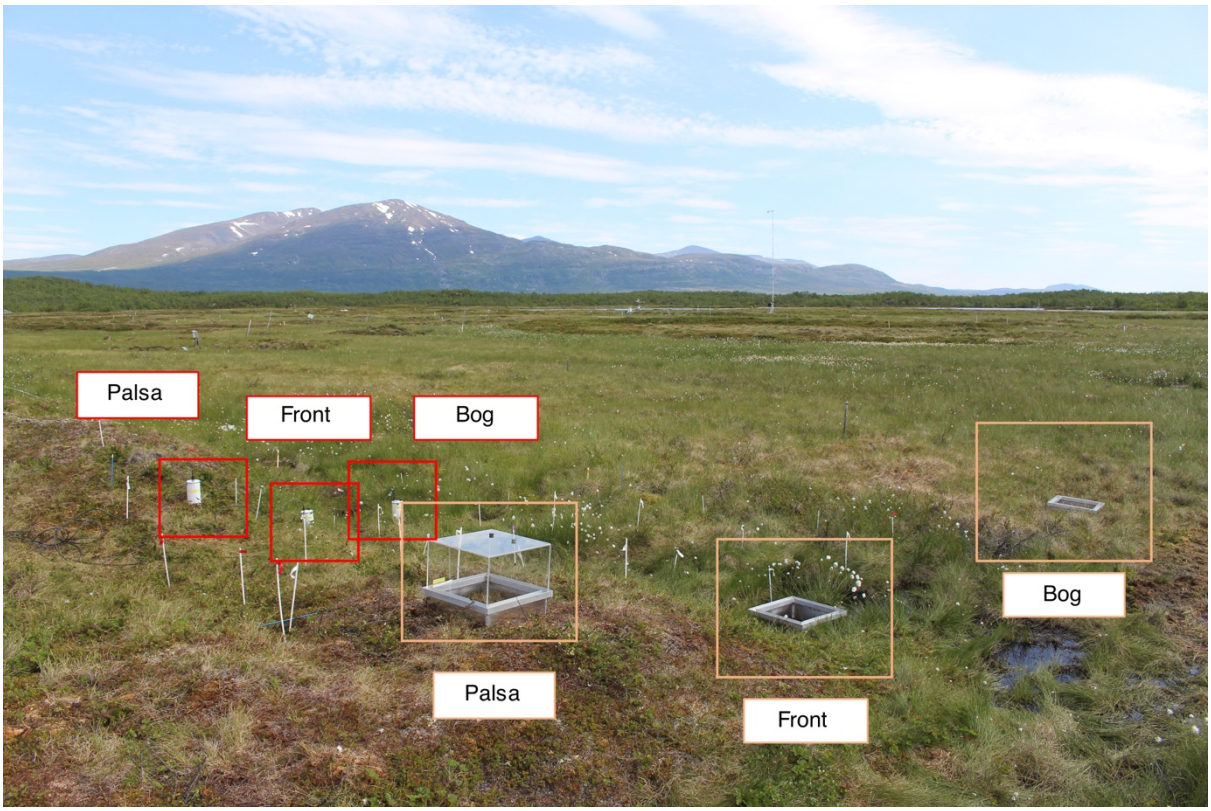

Figure S2. Gas sampling along palsa hillslopes. In transect 1 (see also Figure S1), Eosense gas chambers (eosFD Forced Diffusion chamber in conjunction with the eosLink-FD software, EOSENSE INC, Dartmouth, Canada) (red) were installed to measure carbon dioxide emissions along the palsa hillslope (68°21'18.70"N, 19° 2'38.00"E). Additional gas chambers with plastic chambers, sealed with a rubber stopper, and metal frames (orange) were installed to obtain replicate carbon dioxide and additionally methane emissions along the palsa hillslope into the bog area.

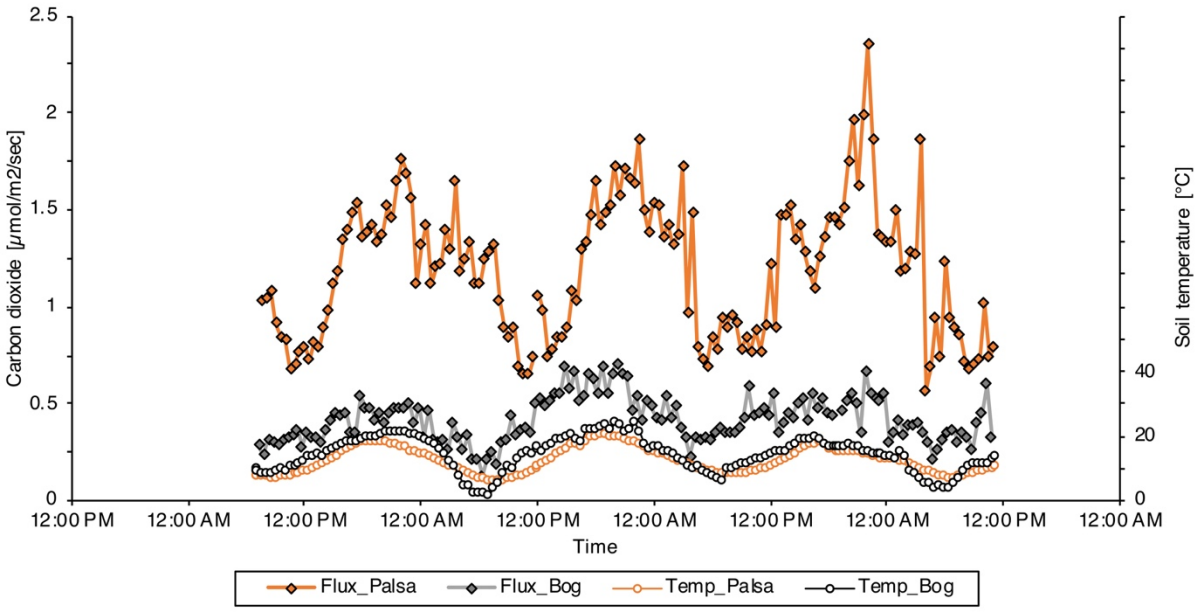

947

948

949 **Figure S3. Carbon dioxide emissions along the palsa hillslope (palsa and bog).** Eosense gas
950 chambers (eosFD Forced Diffusion chamber in conjunction with the eosLink-FD software,
951 EOSENSE INC, Dartmouth, Canada) were installed along the palsa hillslope and analysis
952 performed from the 8th of July to 10th of July 2019. Unfortunately, the second Eosense
953 instrument at the collapsing front (shown in Figure S2) was broken during shipment and thus
954 excluded in the analysis. The carbon dioxide emissions correlate with the surface soil
955 temperature (measured at 5 cm soil depth at palsa and bog), measured by Integrated Carbon
956 Observation System (ICOS) Sweden Abisko – Stordalen[1].

957

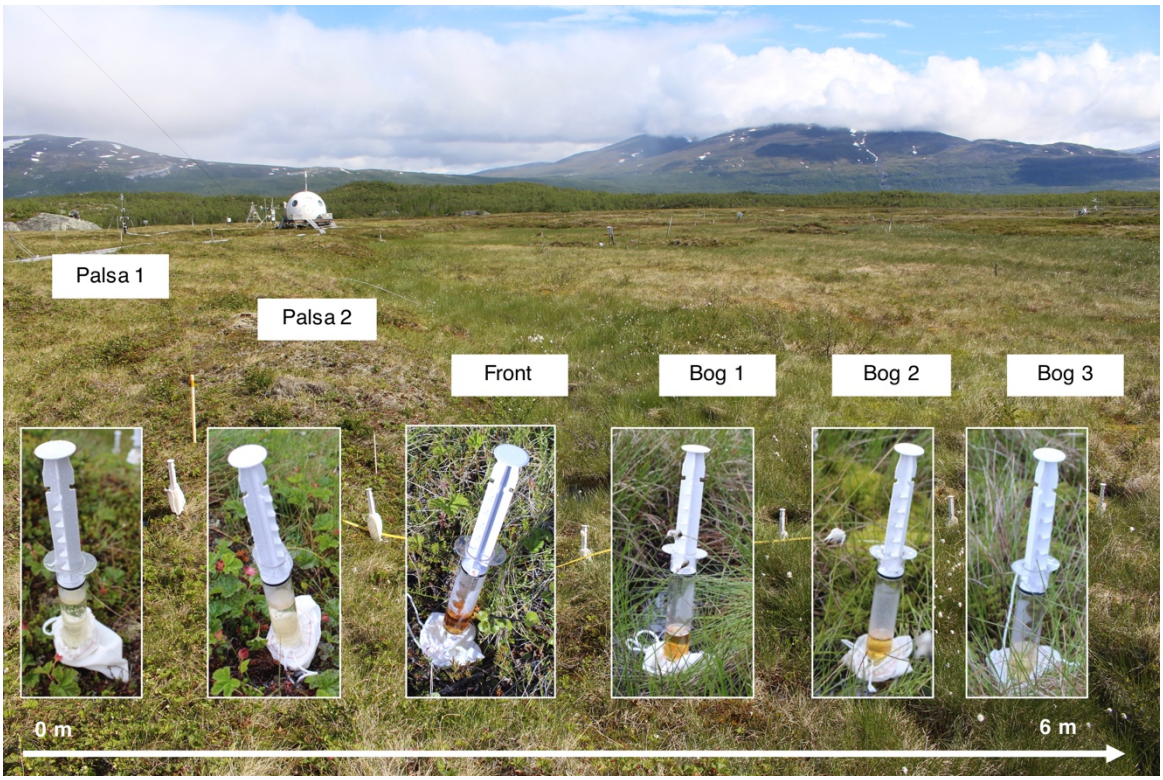

Figure S4. Porewater sampling along palsa hillslopes. Along eight palsa hillslopes, porewater was extracted with lysimeters at six defined sampling points in July 2019. In transect 1 (shown here, see also Figure S1), lysimeters were installed for 3-4 hours along the palsa hillslope (68°21'18.70"N, 19° 2'38.00"E) at a distance of 1 m in between each other from palsa to bog. The porewater with dark brown, reddish color at the collapsing front represents the sample with the highest aqueous iron and dissolved organic carbon along the palsa hillslope into bog.

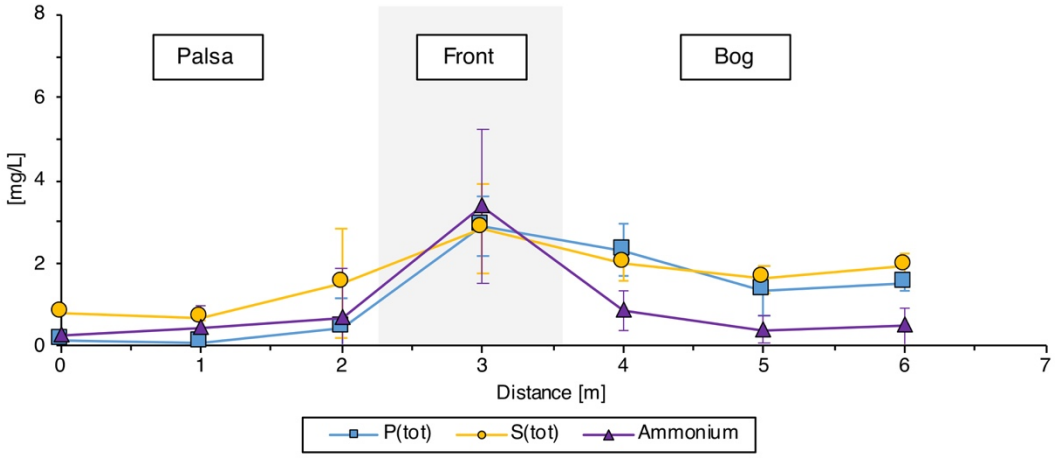

968

969

970 **Figure S5. Aqueous total phosphorous (P(tot)), aqueous total sulfur (S(tot)) and**
971 **ammonium concentrations in the porewater along the palsa hillslope (30 cm depth,**
972 **transition zone).** Aqueous concentrations are reported in mg/L from palsa (0-2.7 m) to bog
973 (2.7-7 m). Reported values represent the average of six sampling spots for eight palsa hillslopes
974 (0-2.3 m) to collapsing front (2.3-3.6 m) to bog (3.6-7 m), sampled in June/July (see also SI,
975 Figures S1 and Figure S4). Error bars represent the standard deviation of eight palsa hillslopes
976 (0-2.3 m) to collapsing front (2.3-3.6 m) to bog (3.6-7 m), sampled in June/July (see also SI,
977 Figure S1).

978

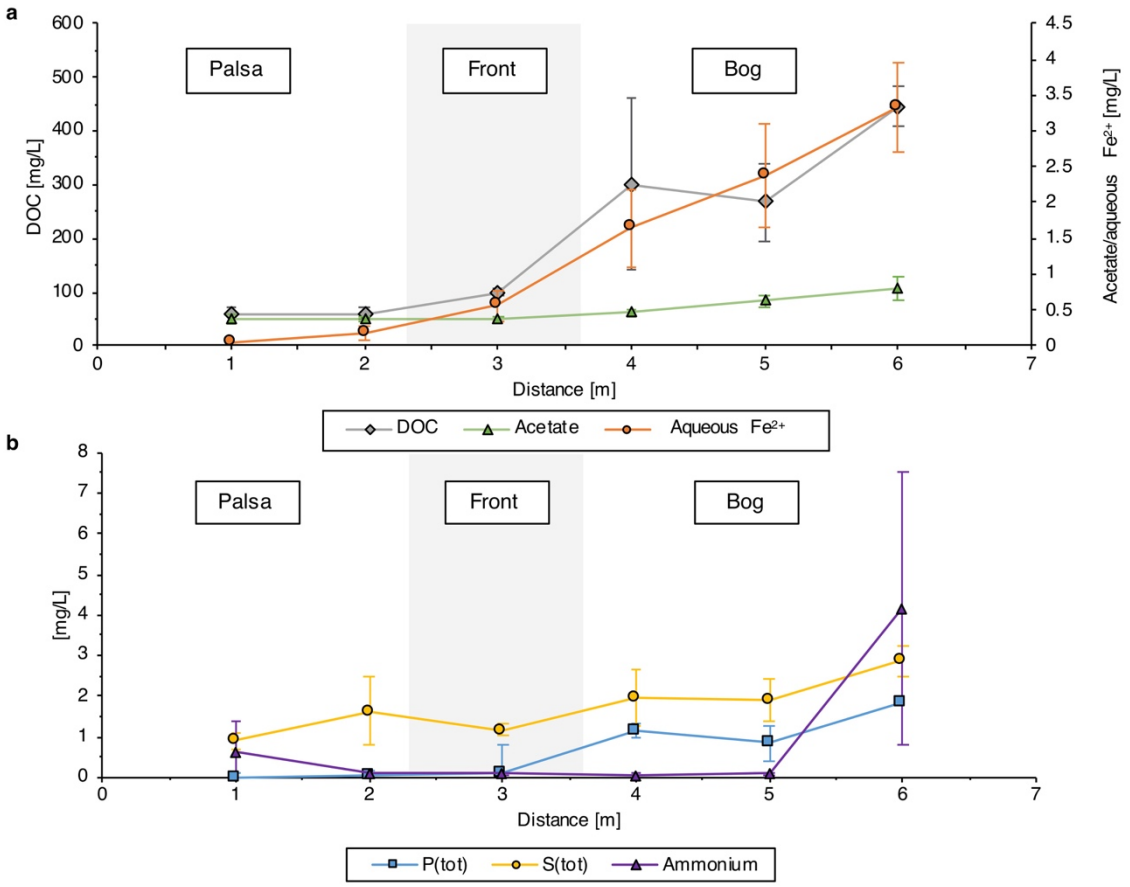

Figure S6. Porewater analysis along the palsa hillslope (60 cm, mineral horizon). a, Dissolved organic carbon (DOC), acetate and aqueous Fe^{2+} in mg/L and b, aqueous total phosphorous (P(tot)), aqueous total sulfur (S(tot)) and ammonium concentrations along the collapsing palsa hillslope into bog. Reported values represent the average of six sampling spots for eight palsa hillslopes (0-2.3 m) to collapsing front (2.3-3.6 m) to bog (3.6-7 m), sampled in June/July (see also SI, Figure S1). Error bars represent the standard deviation of eight palsa hillslopes (0-2.3 m) to collapsing front (2.3-3.6 m) to bog (3.6-7 m), sampled in June/July (see also SI, Figure S1).

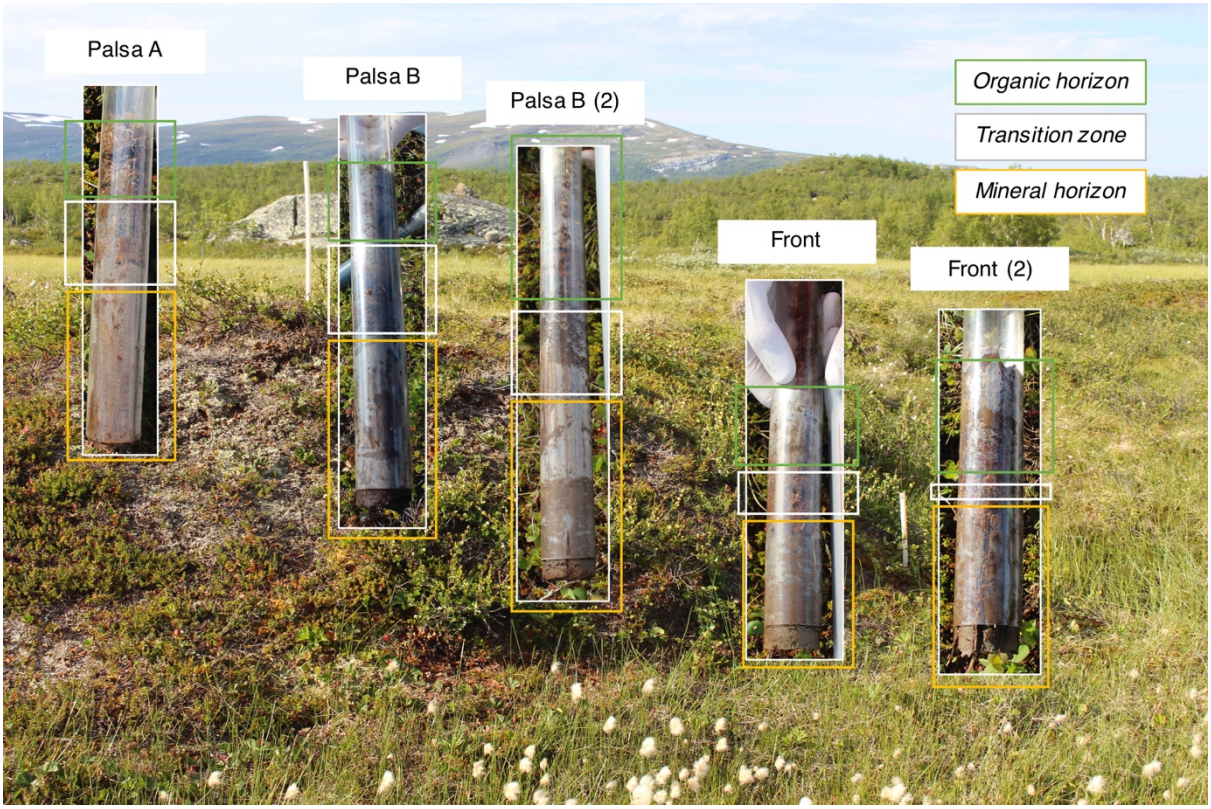

Figure S7. Coring along palsa hillslopes. Ten soil cores were taken along different palsa hillslopes to capture spatial heterogeneity of iron-carbon associations along the peatland mire. In transect 3 (shown here, see also Figure S1), five cores were taken along a palsa hillslope towards the collapsing front into bog (68°21'27.33"N, 19° 3'1.91"E), immediately frozen in liquid nitrogen and stored at -80°C until analysis of iron-carbon associations and of present and active microbial community.

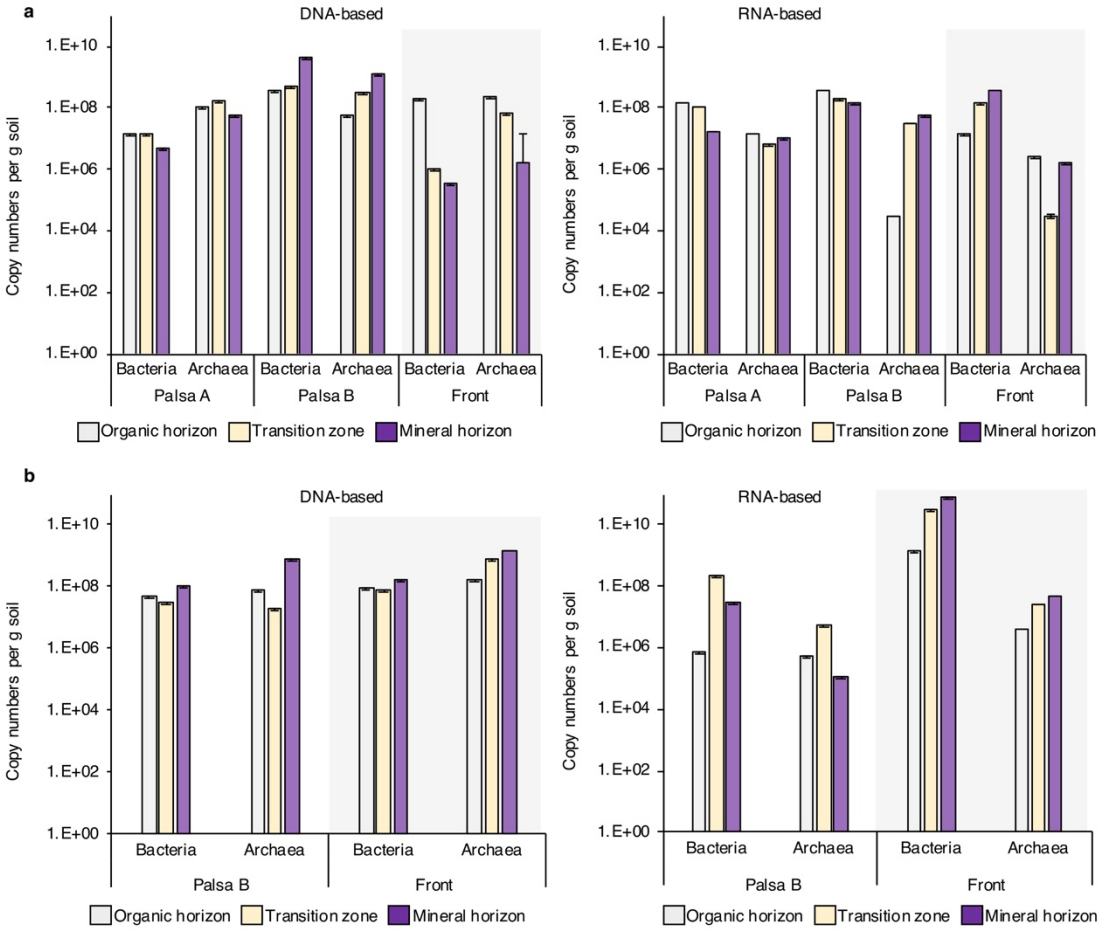

Figure S8. Abundance of bacteria and archaea (copy numbers based on qPCR analysis specific for 16S rRNA genes; DNA-based on the left, RNA-based on the right). a, and b, show replicate analysis for Palsa A, Palsa B and Front (a), and Palsa A and Front (b).

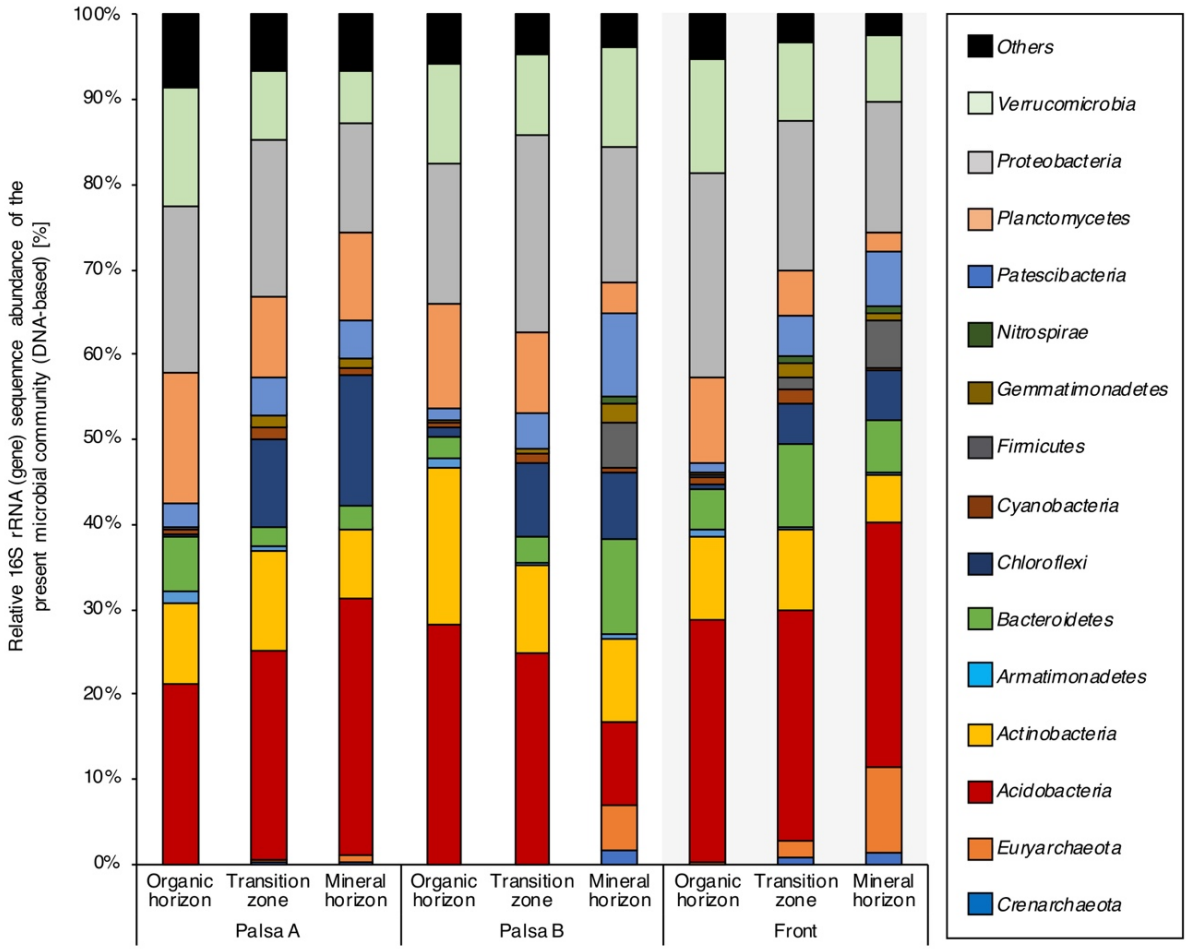

Figure S9 Taxonomic identification of the microbial communities along the palsa hillslope based on 16S rRNA gene amplicon analysis (DNA-based). Data were averaged among triplicate analysis of each soil horizon (organic horizon, transition zone, mineral horizon).

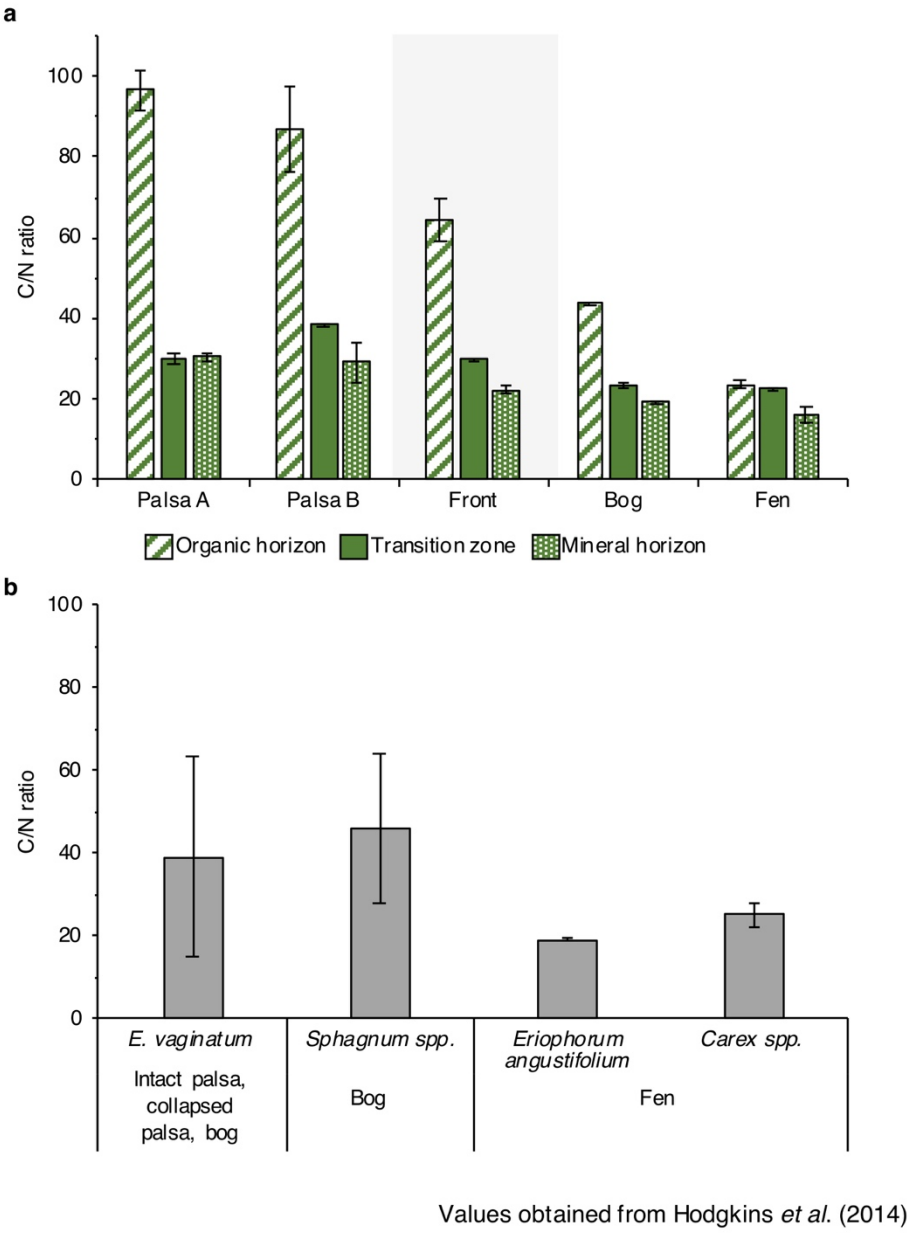

1013

1014

1015 **Figure S10. C/N weight ratios of a, soil samples of distinguished soil horizon along palsa**
1016 **hillslope and thaw gradient, in comparison to b, living plant samples of dominant**
1017 **Stordalen species (modified and adapted from Hodgkins *et al.*[2]).** Reported values represent
1018 the average of triplicate analysis of cores Palsa A, Palsa B, Front (transect 1, Figure S1) and
1019 Bog C and Fen E, which were previously puplished[3]. Error bars represent the standard deviation
1020 of triplicate analysis of cores Palsa A, Palsa B, Front (transect 1, Figure S1), one bog (Bog C)
1021 and one fen core (Fen E) (see also Patzner *et al.*[3]).

1022

1023 **Table S1. Overview of iron(II)-oxidizing microorganisms that were cross-checked in the**
1024 **16S rRNA amplicon gene sequencing results (DNA- and RNA-based) in this study** (adapted
1025 from Otte *et al.*[4] and Weber *et al.*[5], see also Dinh *et al.*[6] and Berg *et al.*[7]).

1026

Iron(II)-oxidizing microorganisms (species or strains)
Acidianus brierleyi
Acidiplasma aeolicum; A. cupricumulans
Acidimicrobium ferrooxidans sp. strain DSM 10331
Acidithiobacillus ferrooxidans sp. strain ATCC 23270
Acidovorax sp. strains 2AN, BoFeN1, BrG1; *A. delafieldii*; *A. ebreus* strain TPSY
Alicyclobacillus disulidooxidans; A. tolerans
Aquabacterium sp. strains BrG2, HidR2
Azoarcus sp. strain ToN1
Azospira sp. strain TR1; *A. oryzae*
Bradyrhizobium japonicum sp. strains 22, in8p8, wssI4
Candidatus Brocadia sinica
Candidatus Scalindua sp.
Chlorobium luteolum DSM273; *C. ferrooxidans* sp. strain KoFox
Chromobacterium violaceum sp. strain 2002
Citrobacter freundii sp. strain PXL1
Comamonas sp. strain MPI12
Crenothrix sp. #
Cupriavidus necator sp. strains A5-1, ss1-6-6
Dechlorobacter hydrogenophilus sp. strain LT-1
Dechloromonas sp.; D. agitata sp. strains CKB, is5; *D. aromatica* sp. strains RCB, UWNR4; *D. suillum* sp. strain PS
Dechlorospirillum sp. strain M1
Denitromonas indolicum
Desulfitobacterium frappieri sp. strain G2
Desulfobacterium corrodens (Dinh *et al.*, 2004)
Escherichia coli sp. strain E4
Ferrimicrobium acidiphilum
Ferriphaselus amnicola (Siderooxydans)
Ferrithrix thermotolerans
Ferritrophicum radicicola
Ferroglobus placidus sp. strain AEDII12DO
Ferroplasma acidarmanus sp. strain fer1
Ferrovibrio denitrificans
Gallionella capsiferriformans; G. ferruginea; G. strain ES-2
Geobacter metallireducens sp. strain GS-15
Geothrix spp.
Hoeflea marina; *H. siderophila* sp. strain Hf1
Hyphomicrobium sp.

(Table continues on next page)

1027

1028

Hyphomonas sp.
Klebsiella-like sp. strain FW33AN
Leptospirillum ferrooxidans; L. ferriphilum
Leptothrix cholodnii; L. discophora
Magnetococcus sp. (Berg *et al*., 2016)
Magnetospirillum bellicus sp. strain VDY
Marinobacter aquaeolei sp. strain VT8
Mariprofundus ferrooxidans sp. strains PV-1, RL-1, JV-1, GSBS
Metallosphaera sedula sp. strain J1
Nocardioides sp. strain In31
Paracoccus sp.*; P. denitrificans; P. ferrooxydans* sp. strain BDN-1*; P. pantotrophus; P. versutus*
Parvibaculum sp. strain MBN-A2
Pedomicrobium spp.
Propionivibrio militaris sp. strain MP
Pseudogulbenkiania ferrooxidans sp. strain 2002
Pseudomonas sp. strains LP-1, SZF15; *P. stutzeri*
Ralstonia solanacearum sp. strain in4ss52
Rhodanobacter sp. strain MPN-A3
Rhodobacter sp. strain SW2*; R. ferrooxydans*
Rhodomicrobium vannielii
Rhodopseudomonas palustris strain TIE-1
Rhodovulum sp.*; R. iodosum; R. robiginosum*
Rubrivivax group sp. strains BrG4, BrG5
Siderocapsa sp.
Sideroxydans paludicola; S. lithotrophicus sp. strain ES-1
Sphaerotilus natans sp. strain DSM 6575
Sulfobacillus spp.
Sulfolobus acidocaldarius
Thauera aromatica sp. strain AR-1
Thermomonas sp. strain BrG3
Thiobacillus denitrificans
Thiodictyon sp.
Thiomicrospira denitrificans
Zixibacteria sp. strain RBG-1

Crenothrix is most often associated with methanotrophy but there are also hints for Fe(II) oxidation.

1031 **Table S2. Overview of iron(III)-reducing microorganisms that were cross-checked in the**
1032 **16S rRNA amplicon gene sequencing results in this study** (adapted from Otte *et al.*[4] and
1033 Weber *et al.*[5], see also Berg *et al.*[7], Li *et al.*[8], Holmes *et al.*[9], Finneran *et al.*[10]).

1034

Iron(III)-reducing microorganisms (species or strains)
Acidithiobacillus ferrooxidans
Aeromonas hydrophila
Albidoferax ferrireducens
Alteromonas hydrophila
Anaeromyxobacter sp.
Bacillus infernus
Clostridium sp.
Deferribacter thermophilus
Desulfobacter propionicus
Desulfobacterium sp.
Desulfobulbus spp.
Desulfococcus spp.
Desulfotalea spp.
Desulfotomaculum sp. (Berg *et al.*, 2016)
Desulfovibrio sp. *(*Li *et al., 2016)*
Desulfuromonas spp.
Desulfuromusa spp.
Ferribacterium limneticum
Ferrimonas balearica
Ferroglobus placidus
Geobacter spp.
Geoglobus sp.
Geothrix fermentans
Geovibrio ferrireducens
Malonomonas sp. (Holmes *et al.*, 2004)
Myxococcales sp.
Pantoea agglomerans sp. strain Sp1
Pelobacter sp.
Pseudomonas sp.
Pseudorhodoferax (Berg *et al.*, 2016)
Pyrobaculum sp.
Rhodobacter sp.
Rhodoferax sp. (Finneran *et al.*, 2003)
Shewanella colwelliana
Sinorhodobacter sp.
Sulfurospirillum barnesii
Thermoterrabacterium ferrireducens
Thermotoga maritima
Thermus sp. strain SA01
Thiobacillus ferrooxidans

1035

1036

Table S3. Overview of methanogenic microorganisms that were cross-checked in the 16S rRNA amplicon gene sequencing results in this study (see also Kim&Whitman[11] and Mondav *et al.*[12]).

Methanogenic microorganisms (genera, species or strains)
Bathyarchaeia
Methanobacterium spp.
Methanobrevibacter spp.
Methanocaldococcus spp.
Methanocella spp.
Methanococcoides spp.
Methanococcus spp.
Methanocorpusculum spp.
Methanoculleus spp.
Methanoflorens spp., *M. stordalenmirensis (Mondav et al., 2014)*
Methanofollis spp.
Methanogenium spp.
Methanohalobium spp.
Methanohalophilus spp.
Methanoignis spp.
Methanolacinia spp.
Methanolinea spp.
Methanolobus spp.
Methanomassillicoccaceae spp.
Methanomethylovorans spp.
Methanomicrobium spp.
Methanoplanus spp.
Methanopyrus spp.
Methanoregula spp.
Methanosaeta spp.
Methanosalsum spp.
Methanosarcina spp.
Methanosphaera spp.
Methanosphaerula spp.
Methanospirillum spp.
Methanothermobacter spp.
Methanothermococcus spp.
Methanothermus spp.
Methanothrix spp.
Methanotorris spp.
Methermicoccus spp.

Table S4. Overview of methanotrophic microorganisms that were cross-checked in the 16S rRNA amplicon gene sequencing results (DNA- and RNA-based) in this study (see also Jiang *et al.*[13] and Singelton *et al.*[14]).

Methanotrophic microorganisms (species or strains)
Acidimethylosilex spp.
Clonothrix spp., *Clonothrix fusca*
Crenotrhix spp., *Crenothrix polyspora*
Methlyosinus spp.
Methyloacida spp.
Methylobacter spp.
Methylobacterium spp.
Methylocaldum spp.
Methylocapsa spp.
Methylocella spp., *Methylocella silvestris*
Methylococcus spp.
Methylocystis spp.
Methylokorus spp.
Methylomonas spp.
Methylosphaera spp.
Methylothermus spp.
Methylovirgula spp.
Rhodoblastus spp.
Roseiarcus spp.

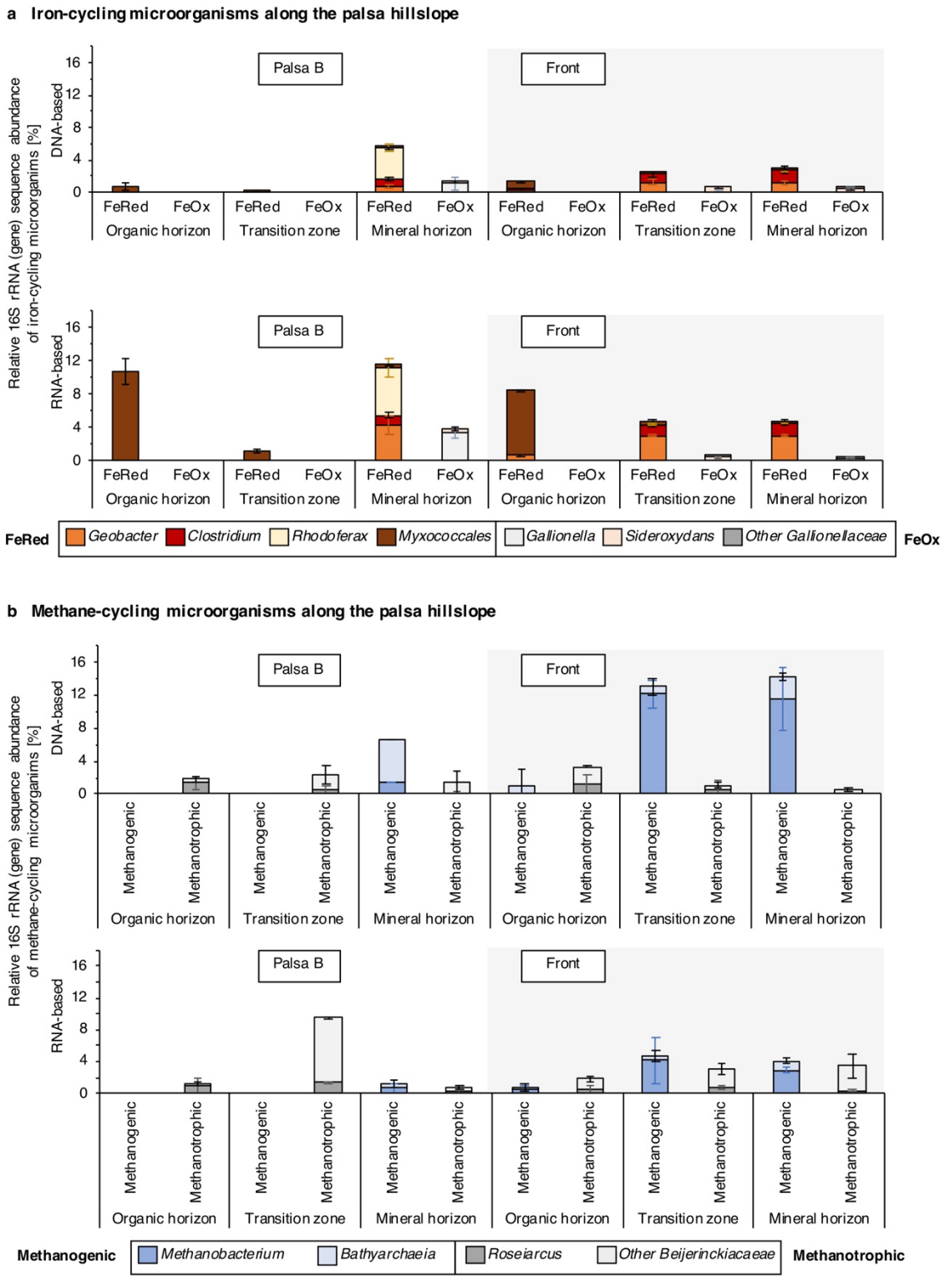

Figure S11. Relative abundance of 16S rRNA (gene) sequence of a, iron- and b, methane cycling microorganisms (DNA- and RNA-based) in replicate cores (Palsa B and Front) along the palsa hillslope (transect 3, Figure 1). All iron- and methane-cycling taxa below 0.1% relative 16S rRNA gene sequencing abundance are not illustrated in this figure. For

absolute abundance of bacteria and archaea based on qPCR analysis, specific for 16S rRNA gene (based on DNA) and Fe- and methane-cycling microorganisms, analyzed in these study (adapted from Otte *et al.*[4] and Weber *et al.*[5]), see also Figure S8. Reported values and error bars represent the average and standard deviation of triplicate analysis of each soil horizon (organic horizon, transition zone and mineral horizon) along the palsa hillslope.

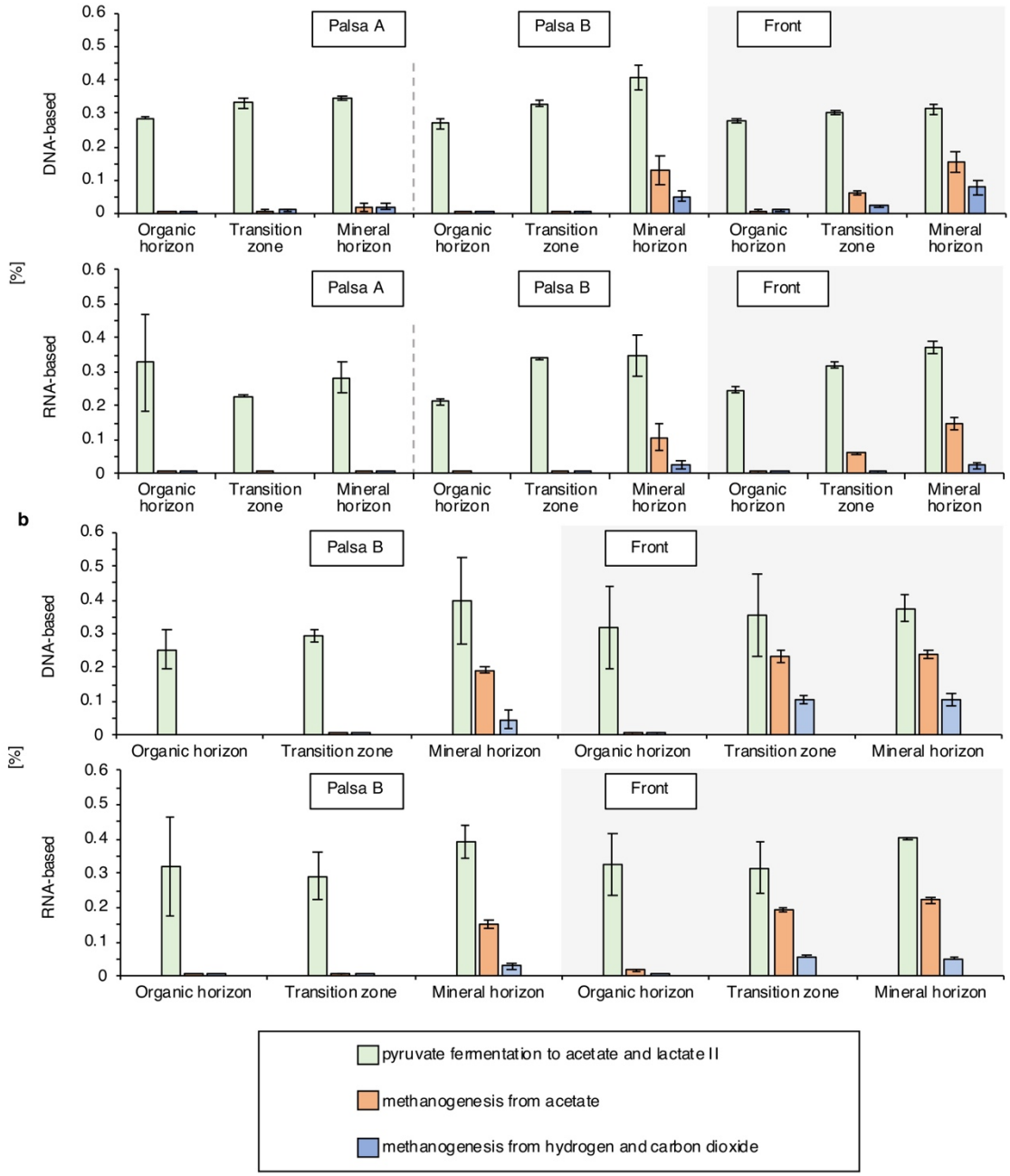

Figure S12. Predicted metabolic pathways of the present (DNA-based) and potentially active (RNA-based) microbial communities along the palsa hillslope in a, cores presented in the main text (transect 3, Figure S1) and b, replicate cores. Analyses were performed with MetaCyc Metabolic Pathway Database. Reported values and error bars represent the average and standard deviation of triplicate analysis of each soil horizon (organic horizon, transition zone and mineral horizon) along the palsa hillslope.

Table S5. Elemental composition percentage and number of FT-ICR-MS assigned formula. Values are derived from total assigned formula tables. Not available (N/A) values for CHNOS formula in porewater samples and salt control extractions are due to lack of reliable formula series detected in those samples. A comparison of the soil extractions using salt or dithionite solutions indicates that the extracts are not identical, but provides little to no evidence of CHOS molecular artifacts formed through reactions with dithionite, as reported by Lv *et al.*[15].

Sample Type	Sample	Extraction	CHO	CHNO	CHOS	CHNOS
			(% abundance / # formula)			
Soil extraction	Palsa A, Transition zone	Dithionite	74.19%/7486	11.21%/2887	13.76%/2018	0.84%/319
		Salt control	58.67%/4952	7.08%/1716	34.25%/6609	N/A
	Front, Transition zone	Dithionite	76.12%/7466	9.25%/2668	14.42%/2881	0.21%/98
		Salt control	76.22%/6536	7.08%/1716	13.79%/2249	N/A
Porewater	Palsa A	N/A	89.79%/9009	7.81%/3374	2.40%/991	N/A
	Front	N/A	87.41%/9072	10.80%/4172	1.79%/984	N/A

Table S6. Absolute values of iron and carbon in locations Palsa A, Palsa B and Front of the cores reported in the main text. Errors of the dithionite/citrate extractable a, iron (reactive Fe, control corrected) and b, carbon (carbon bound to reactive iron, control corrected) represent a combined standard deviation of sodium chloride bicarbonate extractable a, iron and b, carbon, b, citrate blank and dithionite/citrate extractable a, iron and b, carbon (not control corrected).

	Palsa A				Palsa A			
	Reactive Fe [mg/g soil]	Error bars	Associated OC [mg/g soil]	Error bars	Leachable Fe [mg/g soil]	Error bars	Leachable OC [mg/g soil]	Error bars
Organic horizon	0.20	0.12	1.42	1.42	0.05	0.07	2.26	0.45
Transition zone	10.04	0.07	83.69	10.04	0.09	0.07	4.06	0.00
Mineral horizon	3.76	0.48	47.21	14.30	0.05	0.03	2.00	0.19
	Palsa B				Palsa B			
	Reactive Fe [mg/g soil]	Error bars	Associated OC [mg/g soil]	Error bars	Leachable Fe [mg/g soil]	Error bars	Leachable OC [mg/g soil]	Error bars
Organic horizon	0.67	0.07	4.80	0.52	0.00	0.00	3.05	0.71
Transition zone	4.61	0.78	76.60	16.89	0.00	0.00	2.76	0.00
Mineral horizon	4.22	0.09	25.08	4.22	0.00	0.00	0.85	0.00
	Front				Front			
	Reactive Fe [mg/g soil]	Error bars	Associated OC [mg/g soil]	Error bars	Leachable Fe [mg/g soil]	Error bars	Leachable OC [mg/g soil]	Error bars
Organic horizon	0.59	0.30	0.00	0.00	0.07	0.10	2.01	1.11
Transition zone	3.22	0.06	40.88	24.76	0.31	0.01	3.67	0.25
Mineral horizon	3.46	1.40	11.60	8.54	0.63	0.59	1.53	0.47

*Reactive Fe = dithionite extractable Fe - salt extractable Fe (leachable OC)

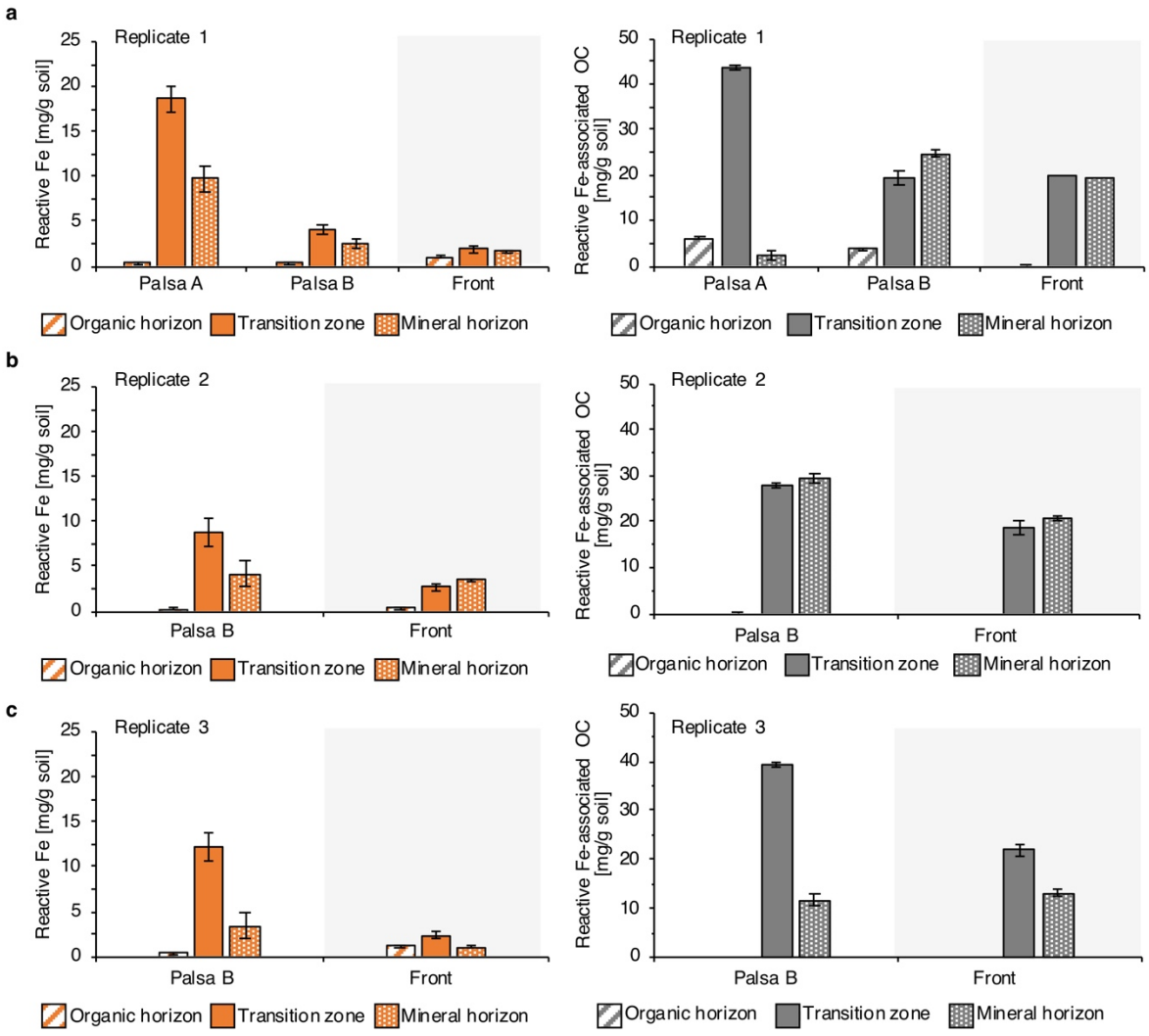

Figure S13. Organic carbon (OC, grey) associated with reactive iron (Fe, orange) along three replicate palsa hillslopes: a, replicate 1 (transect 3), b, replicate 2 (transect 3) and c, replicate 3 (transect 2). Reactive Fe and associated organic carbon along the palsa hillslope (Palsa A, Palsa B and Front) per each soil horizon (organic horizon, transition zone and mineral horizon) [mg/g] decreases towards the collapsing front. Palsa A shows the highest reactive Fe and associated organic carbon in intact permafrost soils. Along the palsa hillslope towards the collapsing front, reactive Fe and associated OC are lost in the solid phase. Reactive Fe reported values are the average of sodium dithionite citrate duplicate extractions of each soil horizon, control corrected by a sodium chloride bicarbonate extractable Fe (leachable Fe). Associated OC reported values are the average of sodium dithionite citrate extractions of each soil horizon, control corrected by the citrate background and the sodium chloride bicarbonate extractable OC (leachable OC) (see also Material and Methods). Cores were taken in July 2019 (see Figure

S1). Error bars of the reactive Fe represent a combined standard deviation of sodium chloride bicarbonate extractable iron and dithionite/citrate extractable Fe. Errors of the associated carbon represent a combined standard deviation of citrate blank, sodium chloride bicarbonate extractable OC and dithionite/citrate extractable OC.

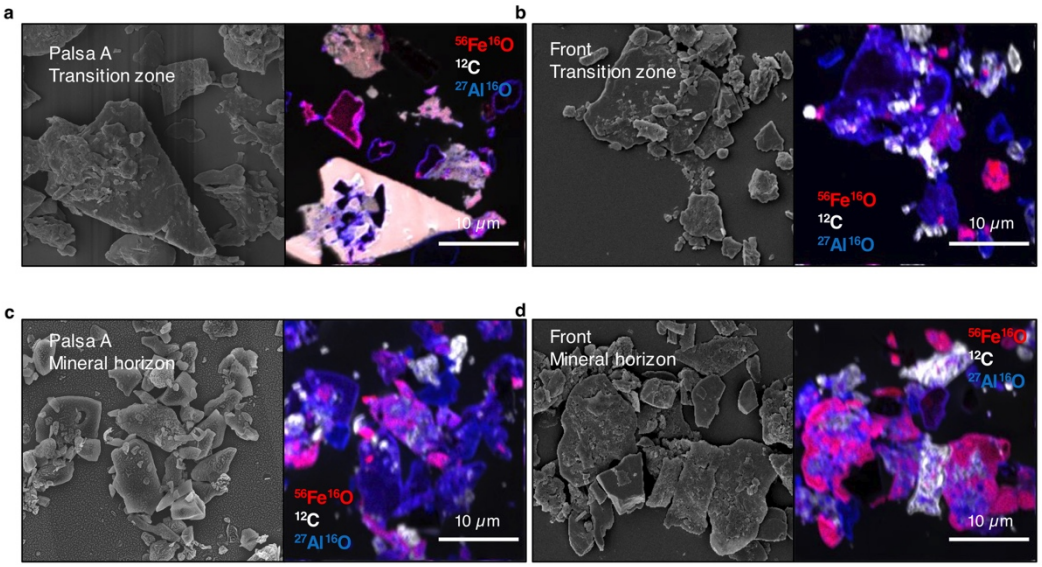

Figure S14. Correlative scanning electron microscopy and nanoscale secondary ion mass spectrometry (nanoSIMS) of fine fraction of palsa soil horizons along the palsa hillslope. Fine particle analysis of a, Palsa A transition zone; b, Front transition zone; c, Palsa A mineral horizon and d, Front mineral horizon (transect 1, Figure S1). Seven detectors were used during nanoSIMS measurements for $^{12}C^-$, $^{16}O^-$, $^{12}C^{14}N^-$, $^{31}P^-$, $^{32}S^-$, $^{27}Al^{16}O^-$ and $^{56}Fe^{16}O^-$ and $^{27}Al^{16}O$. Here, $^{12}C^-$ (white), $^{56}Fe^{16}O^-$ (red) and $^{27}Al^{16}O^-$ (blue) are overlaid in a single composite image.

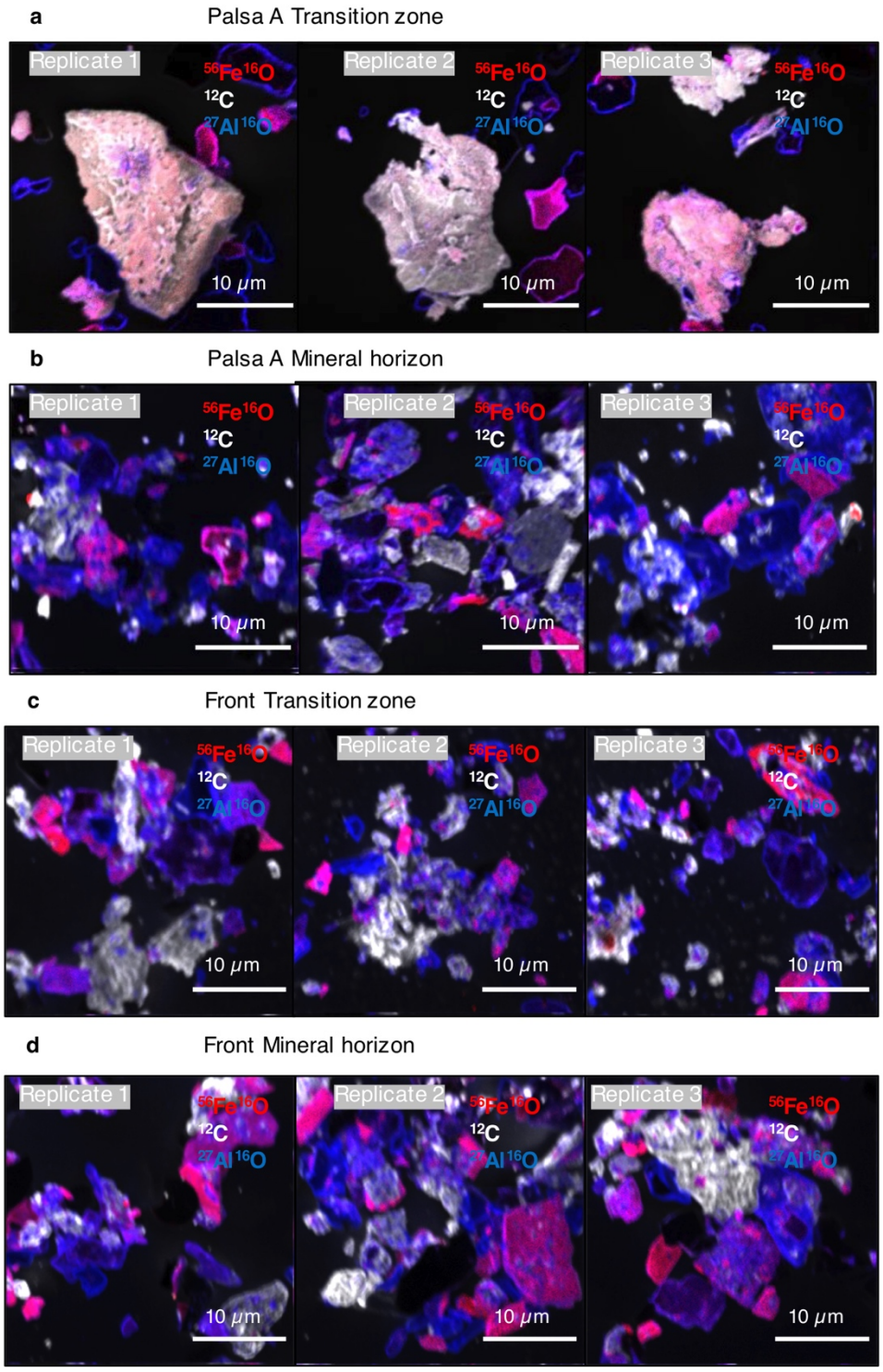

Figure S15. Replicate analysis of nanoscale secondary ion mass spectrometry (nanoSIMS) of fine fraction: a, Palsa A transition zone; b, Palsa A mineral horizon; c, Front transition zone and d, Front mineral horizon (transect 1, Figure S1). Seven detectors were used during nanoSIMS measurements for for $^{12}C^-$, $^{16}O^-$, $^{12}C^{14}N^-$, $^{31}P^-$, $^{32}S^-$, $^{27}Al^{16}O^-$ and $^{56}Fe^{16}O^-$ and $^{27}Al^{16}O$.

Here, $^{12}C^-$ (white), $^{56}Fe^{16}O^-$ (red) and $^{27}Al^{16}O^-$ (blue) are overlaid in a single image. In total, four representative fine particles were analyzed with nanoSIMS.

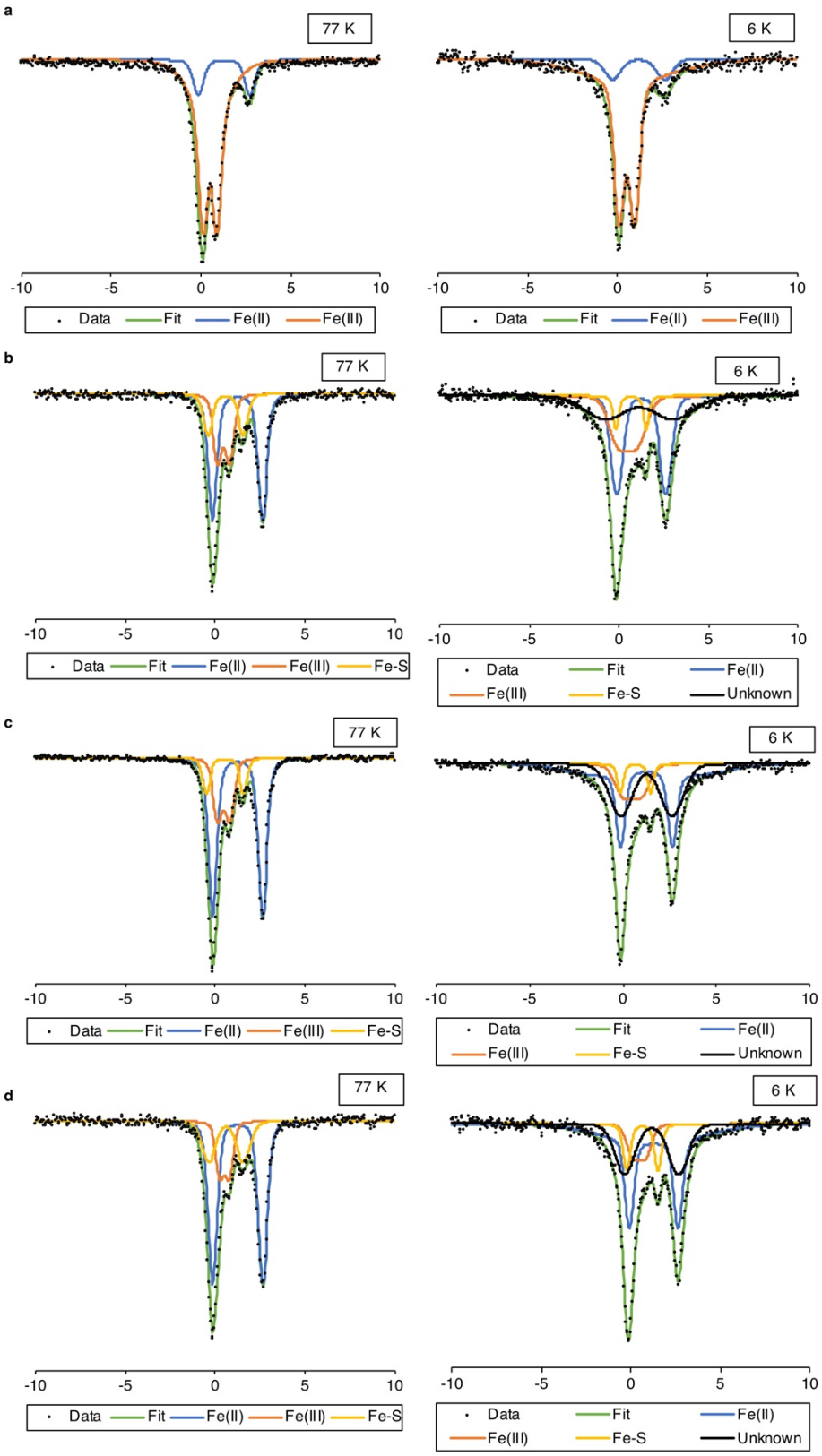

1124

1125

Figure S16. Mössbauer spectroscopy analysis at 77 K and 6 K of the present Fe minerals along the thaw gradient: a, Palsa A transition zone; b, Palsa A mineral horizon; c, Bog (Bog C^3) mineral horizon; d, Fen (Fen E^3) mineral horizon.

1129 **Table S7. Mössbauer spectroscopy parameters (measured at 77 and 6 K)** derived from
1130 fitting spectra obtained for Palsa A transition zone and mineral horizon, Bog (Bog C[3]) and Fen
1131 (Fen E[3]) mineral horizon.

1132

Sample	Components	CS[a] (mm/s)	ΔEQ[b] (mm/s)	σ(Δ)[c] (mm/s)	Bhf[d] (T)	RA[e] (%)	± (%)	χ2 f
77 K								
Palsa A								
Transition zone	Fe(II)	1.28	2.87	0.45	0.00	15.30	0.10	1.77
	Fe(III)	0.50	1.18	1.01	2.06	84.70	0.10	
Palsa A								
Mineral horizon	Fe(II)	1.24	2.79	0.39	0.00	54.46	0.97	0.88
	Fe(III)	0.46	0.67	0.35	0.26	27.45	0.91	
	Fe-S	0.58	1.96	0.40	0.00	18.09	0.93	
Bog (Bog C, see Patzner *et al.*, 2020)								
Mineral horizon	Fe(II)	1.25	2.78	0.37	0.00	62.87	0.38	3.47
	Fe(III)	0.47	0.68	0.37	0.31	24.73	0.34	
	Fe-S	0.54	2.07	0.30	0.00	12.40	0.34	
Fen (Fen E, see Patzner *et al.*, 2020)								
Mineral horizon	Fe(II)	1.25	2.79	0.44	0.00	61.30	0.21	0.61
	Fe(III)	0.52	0.54	0.31	0.41	17.30	0.18	
	Fe-S	0.61	1.93	0.67	0.03	21.40	0.22	
6 K								
Palsa A								
Transition zone	Fe(II)	1.17	2.90	0.80	0.00	12.30	0.16	0.85
	Fe(III)	0.52	2.17	2.65	2.26	87.70	0.16	
Palsa A								
Mineral horizon	Fe(II)	1.25	2.73	0.58	0.00	38.10	0.25	0.81
	Fe-S	0.68	1.68	0.19	0.00	6.50	0.16	
	Fe(III)	0.49	1.19	0.79	0.64	26.90	0.27	
	Unknown	1.13	3.87	2.06	0.29	28.50	0.30	
Bog (Bog C, see Patzner *et al.*, 2020)								
Mineral horizon	Fe(II)	1.26	4.07	2.55	1.50	42.10	0.77	0.75
	Fe-S	0.66	1.64	0.22	0.00	6.00	0.18	
	Fe(III)	0.48	1.07	0.70	0.60	15.90	0.34	
	Unknown	1.26	2.77	1.13	0.08	36.00	0.76	
Fen (Fen E, see Patzner *et al.*, 2020)								
Mineral horizon	Fe(II)	1.28	3.65	2.62	2.03	49.20	0.54	0.54
	Fe-S	0.64	1.74	0.27	0.00	10.70	0.27	
	Fe(III)	0.47	0.76	0.48	0.55	11.50	0.27	
	Unknown	1.16	3.02	0.98	0.02	28.50	0.58	

a CS = center shift
b ΔEQ = quadrupole splitting;
c σ(Δ) = standard deviation of quadrupole splitting component d Bhf = hyperfine magnetic field
e RA = Relative abundance
f χ2 = goodness of fit

1133

1134

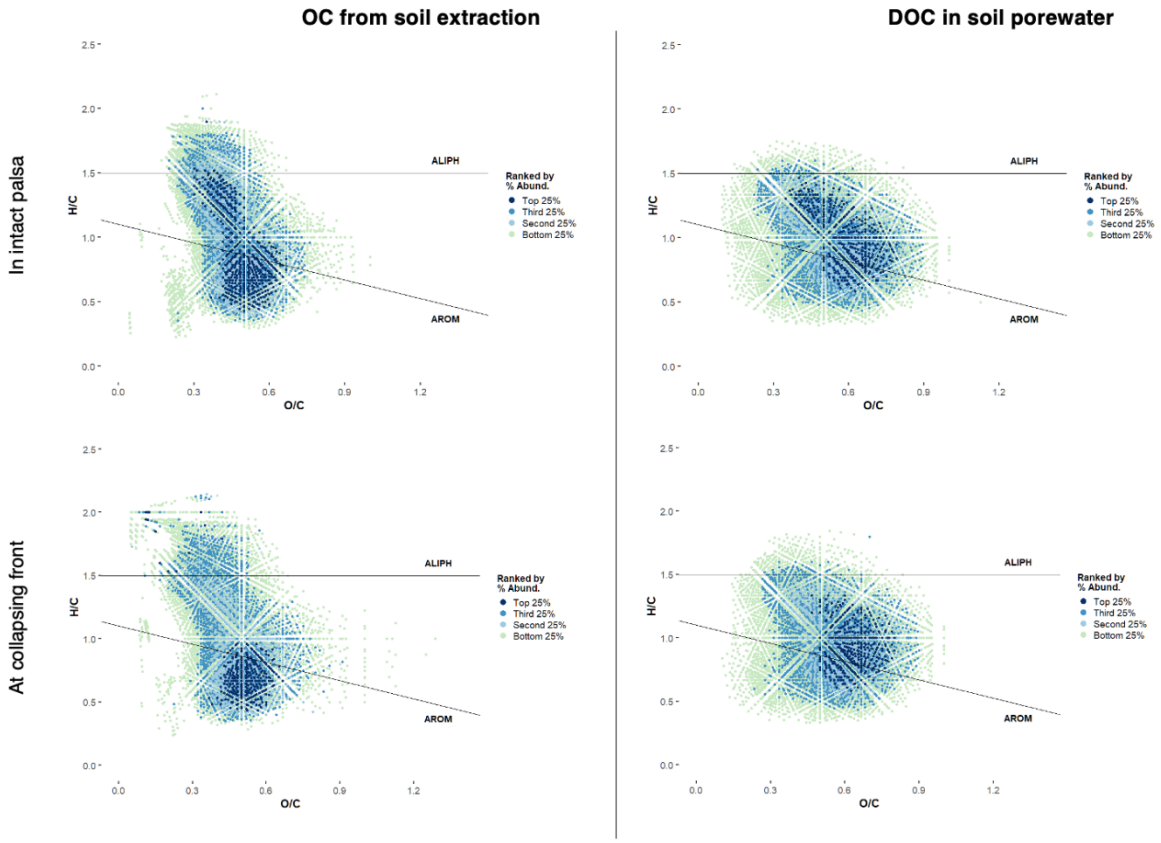

Figure S17. Van Krevelen diagrams for individual samples for solid phase extracted OC (dithionite extractable) from the transition zone of the intact palsa and of the collapsing front (transect 1, Figure S1) and DOC, extracted from 30 cm depth, in intact palsa and at the collapsing front.

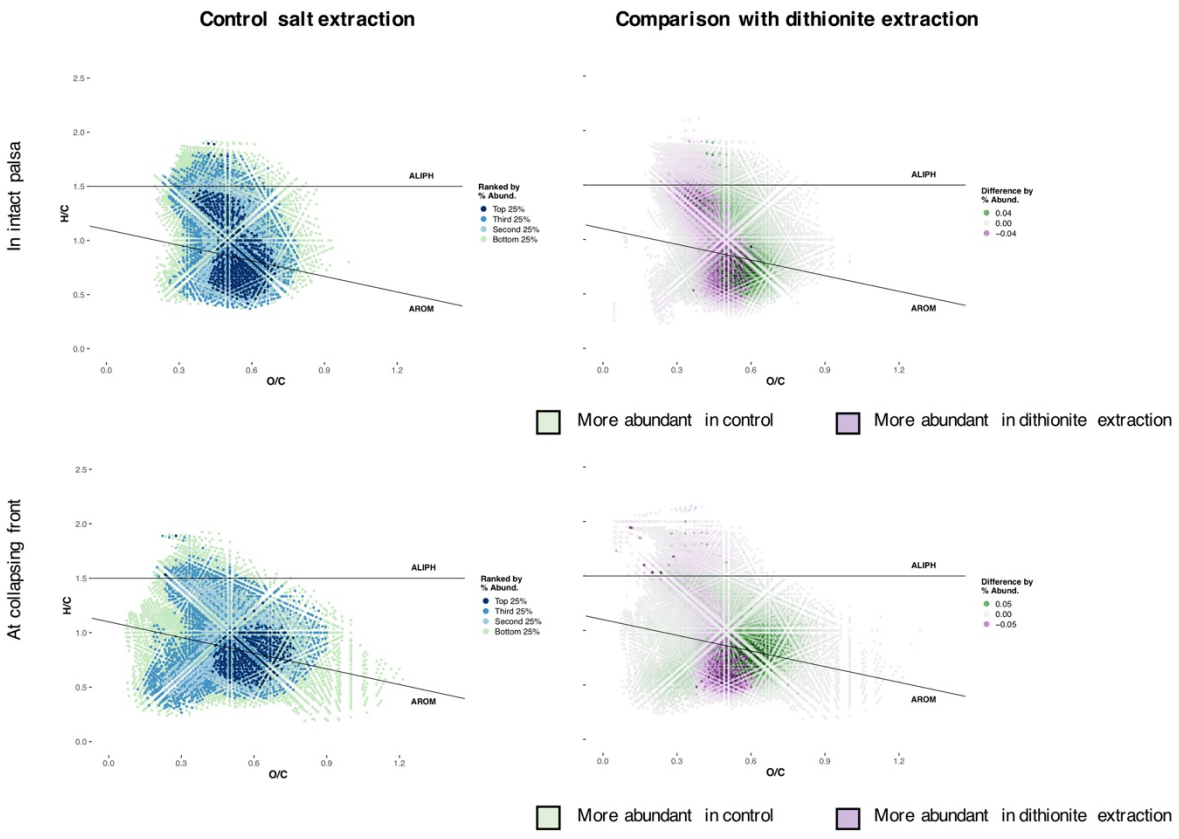

Figure S18. Van Krevelen diagrams of control extractions (sodium chloride bicarbonate with the same ionic strength and pH as the sodium dithionite extraction): left, each individual van Krevelen diagram and right, in direct comparison with the sodium dithionite citrate extractable CHO. Organic carbon (OC) which is more abundant in control (green) represents OC which is leachable of the soil by the same ionic strength and pH as the sodium dithionite extraction. OC which is more abundant in the sodium dithionite extraction (purple) is only dissolved by reductive dissolution.

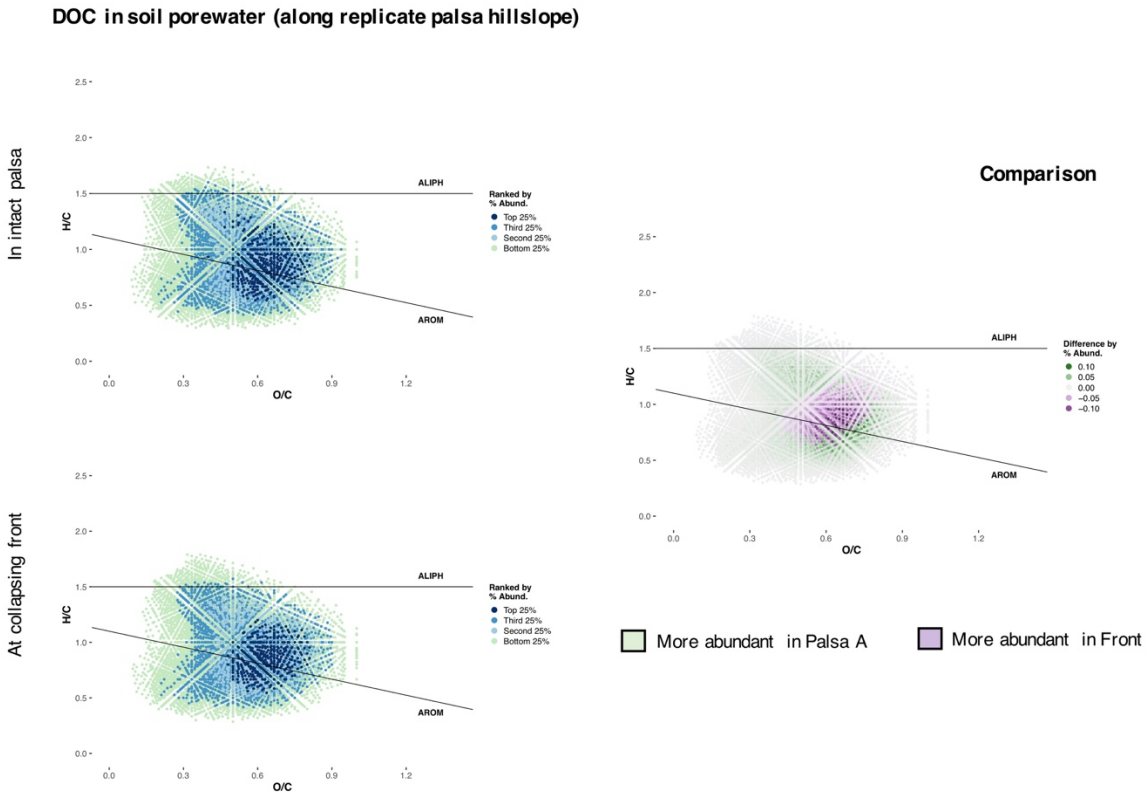

Figure S19. Van Krevelen diagrams for replicate porewater samples (30 cm depth) (left) and in direct comparison to each other (right). Dissolved OC, which is only found in Palsa A, is enriched in more aliphatic compounds (green). Towards Front and Bog, only more aromatic molecules (purple) remain.

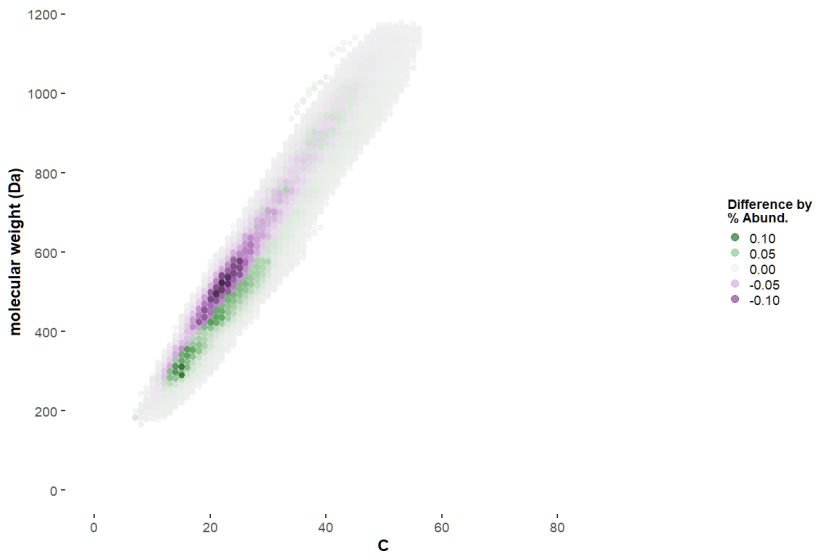

Figure S20. Molecular weight (MW) of dissolved organic carbon compounds in intact palsa versus at the collapsing front. Lower MW compounds have higher relative abundance in porewater samples from intact palsa at a lower molecular weight for a given carbon number (colored in green). Higher MW compounds have higher relative abundance for a given carbon number at the collapsing front (colored in purple).

References:

1 Rinne, J., ICOS Sweden Ecosystem eco time series (ICOS Sweden), Abisko-Stordalen Palsa Bog, 2018-12-31–2019-12-31, https://hdl.handle.net/11676/s5oBzukX_FaXpHU___86QasO) (2021).

2 Hodgkins, S. B. *et al.* Changes in peat chemistry associated with permafrost thaw increase greenhouse gas production. *Proc. Natl. Acad. Sci. USA* **111**, 5819-5824, (2014).

3 Patzner, M. S. *et al.* Iron mineral dissolution releases iron and associated organic carbon during permafrost thaw. *Nat Commun* **11**, 6329 (2020).

4 Otte, J. M. *et al.* The distribution of active iron-cycling bacteria in marine and freshwater sediments is decoupled from geochemical gradients. *Method Enzymol* **20**, 2483-2499 (2018).

5 Weber, K. A., Achenbach, L.A., Coates, J.D. Microorganisms pumping iron: anaerobic microbial iron oxidation and reduction. *Nat. Rev. Microbiol.* **4**, 752-764 (2006).

6 Dinh, H. T., Kuever, J., MussBmann, M., Hassel, A.W. Iron corrosion by novel anaerobic microorganisms. *Nature* **427**, 829 (2004).

7 Berg, J. S., Michellod, D., Pjevac, P., Martinez-Perez, C., Buckner, C.R., Hach, P.F. Instensive cryptic microbial iron cycling in the low iron water column of the meromictic Lake Cadagno. *Method Enzymol* **18**, 5288-5302 (2016).

8 Li, X., Zhang, W., Liu, T., Chen, L., Chen, P., Li, F. Changes in the composition and diversity of microbial communities during anaerobic nitate reduction and Fe(II) oxidation at circumneutral pH in paddy soil. *Soil Biol Biochem* **94**, 70-79 (2016).

9 Holmes, D., Bond, D., O'neil, R., Reimers, C., Tender, L., Lovely, D. Microbial communities associated with electrodes harvesting electricity from a variety of aquatic sediments *Microb Ecol* **48**, 178-190 (2004).

10 Finneran, K. T., Johnsen, C.V., Lovely, D.R. Rhodoferax ferrireducens sp. nov., a psychotolerant, facultatively anaerobic bacterium that oxidizes acetate with the reduction of Fe(III). *Inst J Syst Evol Microbiol* **53**, 669-673 (2003).

11 Kim, W., Whitman, W.B. Methanogens. *Encyclopedia of Food Microbiology (Second Edition), Academic Press, ISBN 9780123847331*, 602-606 (2014).

12 Mondav, R. *et al.* Discovery of a novel methanogen prevalent in thawing permafrost. *Nat Commun* **5**, 3212 (2014).

13 Jiang, H., Chen, J.C., Murrell, P., Jiang, C., Zhang, C., Xing, X.-H., Smith, T.J. . Methanotrophs: Multifunctional bacteria with promising applications in environmental bioengineering. *Comprehensive Biotechnology (Second Edition), Academic Press, ISBN 9780080885049*, 249-262 (2011).

14 Singelton, C. M. *et al.* Methanotrophy across a natural permafrost thaw environment *The ISME Journal* **12**, 2544-2558 (2018).

15 Lv, J., Huang, Z., Christie, P., Zhang, S. Reducing reagents induce molecular artifacts in the extraction of soil organic matter. *ACS Earth and Space Chem* **4** (11), 1913-1919 (2020).